



**HAL**  
open science

## On the chemical composition and structure of incipient soot in a laminar diffusion flame

Jessy Elias, Alessandro Faccinetto, Cornelia Irimiea, Nicolas Nuns, Claire Pirim, Cristian Focsa, Hervé Vezin, Xavier Mercier

► **To cite this version:**

Jessy Elias, Alessandro Faccinetto, Cornelia Irimiea, Nicolas Nuns, Claire Pirim, et al.. On the chemical composition and structure of incipient soot in a laminar diffusion flame. *Fuel*, 2024, 373, pp.132056. 10.1016/j.fuel.2024.132056 . hal-04621441

**HAL Id: hal-04621441**

**<https://hal.science/hal-04621441v1>**

Submitted on 8 Nov 2024

**HAL** is a multi-disciplinary open access archive for the deposit and dissemination of scientific research documents, whether they are published or not. The documents may come from teaching and research institutions in France or abroad, or from public or private research centers.

L'archive ouverte pluridisciplinaire **HAL**, est destinée au dépôt et à la diffusion de documents scientifiques de niveau recherche, publiés ou non, émanant des établissements d'enseignement et de recherche français ou étrangers, des laboratoires publics ou privés.

1 On the chemical composition and structure of  
2 incipient soot in a laminar diffusion flame

3 *J. Elias<sup>1,2</sup>, A. Faccinetto<sup>1,\*</sup>, C. Irimiea<sup>3</sup>, N. Nuns<sup>4</sup>, C. Pirim<sup>5</sup>, C. Focsa<sup>5</sup>, H. Vezin<sup>6</sup>, X. Mercier<sup>1</sup>*

4 *<sup>1</sup>Univ. Lille, CNRS, UMR 8522, PC2A, F-59000 Lille, France*

5 *<sup>2</sup>ADEME, F-49004, Angers, France*

6 *<sup>3</sup>DMPE, ONERA, Univ. Paris Saclay, F-91123 Palaiseau, France*

7 *<sup>4</sup>Univ. Lille, M. E. Chevreul Institute, F-59000 Lille, France*

8 *<sup>5</sup>Univ. Lille, CNRS, UMR 8523, PhLAM, F-59000 Lille, France*

9 *<sup>6</sup>Univ. Lille, CNRS, UMR 8516, LASIRE, F-59000 Lille, France*

10 *\*Corresponding author*

11

12     **Abstract**

13     The transformation of molecular precursors in the gas phase into nanoparticles in the condensed phase  
14 (*soot inception*) during combustion has not yet been fully understood. While several hypotheses on soot  
15 inception are currently being examined, their validation requires detailed knowledge of the  
16 physical-chemical properties of the matter first formed in the condensed phase (*incipient soot*). However,  
17 characterizing short-lived species in a reactive environment at high temperature is inherently difficult. In  
18 this work, we propose a multi-analytical approach to indirectly characterize chemical composition and  
19 structure of incipient soot obtained in controlled laboratory conditions. The results are explained in light  
20 of recent developments on the characterization of the optical and magnetic properties of incipient soot,  
21 and used to build a phenomenological model of soot inception. The acquired information is key to support  
22 the hypothesis selection and to understand the reactivity of combustion byproducts and thus their impact  
23 on health and the environment.

24     **Keywords**

25     Soot inception, incipient soot, multi-diagnostics characterization, structure, chemical composition,  
26 diffusion flames, ToF-SIMS, Raman spectroscopy.

27

## 28 **1. Introduction**

29 Soot is made of fractal-like aggregates of carbonaceous nanoparticles formed during the incomplete  
30 combustion of hydrocarbons. A vast body of literature has been devoted to understanding the fundamental  
31 mechanisms governing the transition from the gas to the condensed phase (*soot inception*) in hydrocarbon  
32 flames. As a result, a number of hypotheses on the main mechanisms of soot inception are currently being  
33 under validation by the scientific community [1–6]. Incipient soot is defined as the matter first formed in  
34 the condensed phase from molecular precursors like polycyclic aromatic hydrocarbons (PAHs) and their  
35 derivatives [7]. Over the years, it became clear that detailed knowledge of the physical-chemical  
36 properties of incipient soot is key to understand soot inception. However, it also became evident that  
37 many physical-chemical properties of incipient soot significantly differ from mature soot. In addition to  
38 being fundamental for the hypothesis selection, these differences affect the interpretation of the output of  
39 several diagnostics, and therefore must be considered for the accurate interpretation of the experimental  
40 data.

41 During the last two decades, a remarkable number of investigations on the formation and  
42 characterization of incipient soot have been published, most focusing on the soot nanoparticles size  
43 distribution and structure. Unlike primary particles that can reach diameters up to tens of nanometers and  
44 are characterized by a classic core-shell internal nanostructure [8,9], incipient particles can be as small as  
45 1-3 nm [10,11] and appear to be constituted of 2-3 atomic layers [12] of either amorphous or randomly  
46 oriented carbonaceous clusters [13–15]. The core of primary particles has been shown to be compatible  
47 with the coagulation of 2-3 incipient particles [8,16], suggesting that incipient particles may grow into  
48 primary particles. However, the coagulation rate of incipient particles in flames is generally sufficiently  
49 low [17–19] that they can coexist and be detected along with larger particles [20–24].

50 The specific heat capacity and density [25] and the complex refractive index function [26–29] of  
51 incipient soot are significantly lower than mature soot. Incipient soot is characterized by weak absorption

52 in the visible light spectrum, and lack the strong thermal radiation emission that can be fitted with  
53 Planck's law typical of mature soot [30,31].

54 In contrast, little and mostly indirect information on the chemical composition and structure of incipient  
55 soot is currently known. Implementing the diagnostics required to detect and analyze short-lived species  
56 or nanoparticles in a complex reactive environment at high temperature and interpreting the resulting data  
57 is a challenging task, especially since sampling is required for online and ex situ analyses. Incipient soot  
58 is richer in small PAHs [32] and aliphatics [33,34] than mature soot, although significant differences exist  
59 between diffusion and premixed flames [35]. Direct evidence on the structure of isolated molecules  
60 thermally desorbed from incipient soot has been recently produced [36,37]. The higher H/C ratio  
61 [9,38,39] and smaller particle size [14,40] of incipient soot result in different chemical reactivity [41–43]  
62 and hygroscopic properties [44,45] than mature soot.

63 To address this lack of fundamental knowledge, in this work we present the fine characterization of the  
64 chemical composition and structure of incipient soot generated in a co-flow laminar diffusion flame of  
65 methane. This flame has already been extensively characterized in our previous works using different in  
66 situ and ex situ diagnostics (*Methods* 2.1-2.2). The soot and PAH regions have already been mapped in  
67 situ, and used to select the sampling points that are investigated in this work by time of flight secondary  
68 ions mass spectrometry (ToF-SIMS, *Methods* 2.3) and Raman spectroscopy (*Methods* 2.4-2.5). The data  
69 analysis and interpretation rely on principal component analysis (PCA, *Methods* 2.6) to infer information  
70 on the properties of incipient soot: the principal components representative of the chemical composition  
71 and of the structure are first identified (*Results* 3.1-3.4), then cross-compared (*Results* 3.5), and finally  
72 correlated to the data obtained in situ or already available in the literature in a thorough multi-diagnostic  
73 approach (*Discussion* 4.1). In particular, the atomic fraction of hydrogen obtained from the analysis of the  
74 mass spectra [35] has been suggested to be linked to the formation rate of covalent C-C bonds [46]. The  
75 structure of incipient soot is derived from the detailed analysis of the Raman spectra and is shown to  
76 evolve as a function of the appearance of curved graphene layers, the presence of finite-size carbon  
77 crystallites, and the changing distance between graphene-like layers. These results are discussed in the

78 framework of the recent advancements in the characterization of the concentration and structure of  
79 persistent radicals in incipient soot [47], and more specifically of our recent electron paramagnetic  
80 resonance (EPR) measurements [48]. The cross-examination of these properties allows the identification  
81 of several properties of the chemical species involved in the phase transition that are used to propose a  
82 phenomenological model of soot inception (*Discussion 4.2*).

## 83 **2. Materials and methods**

### 84 **2.1 Flame and sampling**

85 The investigated flame is a 120 mm high axisymmetric co-flow laminar methane/air diffusion flame  
86 stabilized on a burner at atmospheric pressure. The burner consists of a central injector supplied with  
87  $0.52 \text{ L min}^{-1}$  of methane and surrounded by an  $86.6 \text{ L min}^{-1}$  air shield (standard  $T$  and  $p$ ). Samples are  
88 extracted from the flame axis using a dilutive quartz microprobe inserted radially into the flame and  
89 operated with nitrogen to reduce the collision probability in the sampling line and quench the reactivity in  
90 the sampled flow. The sampling scheme is shown in the supporting information (SI 8.1) where it is  
91 compared to the mapping of the soot volume fraction obtained by LII as detailed below. The collected  
92 species are deposited on Ti wafers with the same 1/8" diameter impactor used in our previous works  
93 [35,46,49]. High-velocity impaction ( $\sim 34 \text{ m s}^{-1}$ ) results in carbonaceous particles aggregating at the  
94 impaction site at the center of the wafer and in the condensable gas scattering all over the wafer surface  
95 [46]. ToF-SIMS and Raman measurements are performed on two selected ROIs: the materials deposited  
96 directly at the impaction site (impaction ROI), and the materials scattered on the wafer surface  
97 surrounding it (halo ROI).

### 98 **2.2 In situ characterization of the flame**

99 Soot particles have already been mapped using in situ laser induced incandescence (LII) [50]. LII  
100 measurements are performed at 1064 nm using the fundamental of a Nd:YAG laser (Quantel Brilliant B).  
101 The LII is recorded at  $90^\circ$  with respect to the laser beam using a fast ICCD camera (Princeton Instruments

102 PI-MAX2, Roper Scientific). The LII signal is summed over the 580-800 nm spectral range. Soot  
103 particles are heated below the sublimation threshold at  $130 \text{ mJ cm}^{-2}$ .

104 PAHs [50] and OH radicals [51] have already been mapped in this flame using in situ laser induced  
105 fluorescence (LIF). Briefly, LIF measurements are performed at several excitation wavelengths in the  
106 UV-Vis spectral range. The excitation source is a Nd:YAG laser (Quanta-ray, Spectra Physics) used to  
107 pump an optical parametric oscillator (premiScan-ULD/240, GWU-Lasertechnik) to provide tunable  
108 wavelengths at 213-532 nm. The PAH fluorescence spectra, induced at 532 nm, are recorded using a fast  
109 ICCD camera (PI-MAX2, Roper Scientific) coupled to a spectrometer (IHR320, Jobin Yvon). To avoid  
110 any interference with the LII, the laser fluence is set to  $13 \text{ mJ cm}^{-2}$ , which is below the activation  
111 threshold of the LII. The PAH fluorescence is summed over the 550-700 nm spectral range. OH-LIF  
112 spectra are obtained by exciting the A-X (0-0) band (309-312 nm) and by collecting the fluorescence  
113 signal in the R bands spectral range (305-308 nm). The emitted fluorescence is collected at  $90^\circ$  and  
114 imaged with a spectrometer (IHR320, Jobin Yvon) coupled to a photomultiplier tube (XP2020Q,  
115 Photonics). The anti-Stokes collection scheme minimizes potential spectral interferences with the intense  
116 PAHs fluorescence above 300 nm. The results obtained in the previous works are used to establish a  
117 sampling scheme and are critical for the interpretation of the results.

### 118 **2.3 Secondary ions mass spectrometry (ToF-SIMS)**

119  $\text{Bi}_3^+$  primary ions are used to sputter and ionize the species on the samples surface. The secondary ions  
120 are accelerated and analyzed on a time-of-flight mass spectrometer with a maximum resolving power  
121  $m/\Delta m \approx 10^4$  at 200  $m/z$ . This technique is sensitive to high mass organic compounds ( $m/z > 200$ ) due to  
122 the use of primary  $\text{Bi}_3^+$  ions having 25 keV energy with very low current intensity of 0.3 pA (static  
123 mode). Mass spectra in positive polarity are recorded at 50 scans per acquisition on a  $500 \times 500 \mu\text{m}^2$   
124 surface with an image resolution of  $128 \times 128$  pixels. Acquisitions are performed on three different zones  
125 on each ROI, halo and impaction. The information extracted from the mass spectra includes: the  
126 time-of-flight of 520 peaks selected after background and fragment ions removal that is calibrated into

127  $m/z$  and used to identify unknown species, and the peak normalized ion counts  $I_n$  defined as  $I_n = I/I_{TIC}$   
128 where  $I$  is the peak ion count and  $I_{TIC}$  the total relevant ion count (total ion count after background  
129 removal). Peaks are identified using mass defect analysis, allowing the assignment of a molecular formula  
130 to the selected  $m/z$  following the protocol established in our previous works [35,46,49]. The mass spectra  
131 (SI 8.1), the mass defect plot with the complete peak list (SI 8.3) is available in the supporting  
132 information.

133 The atomic fraction of hydrogen [H] is calculated from the mass spectra using the peaks identified by  
134 mass defect analysis, where the normalized signal intensity  $w_i$  is used to weight the individual  
135 contributions of the identified ions  $N_{X,i}$  [46,52]:

$$[H] = \frac{N_H}{N_H + N_C + N_O} \quad \text{Equation 2.1.}$$

With 
$$N_X = \sum_i N_{X,i} w_i, \quad X = H, C, O, \quad \sum_i w_i = 1 \quad \text{Equation 2.2.}$$

136

## 137 **2.4 Raman spectroscopy**

138 The Raman microscope (InVia Reflex, Renishaw) is equipped with a  $\lambda = 514.5$  nm diode-pumped solid  
139 state laser. The laser power is reduced to 0.05%, corresponding to a low laser irradiance of  $1.63 \text{ kW cm}^{-2}$ ,  
140 to avoid structural changes in the sample. The laser beam is focused on the samples with a  $20\times$   
141 magnification objective. The Raman spectral intensity and wavelength are calibrated with a Si wafer by  
142 using the pure Si peak at  $520 \text{ cm}^{-1}$ . The same instrument settings ( $600 \text{ lines mm}^{-1}$  grating, acquisition time  
143 6 s times 80 accumulations per spectrum), chosen after a set of test measurements to provide the best  
144 signal-to-noise ratio for the analysis, are used for all samples. In particular, for samples collected at low  
145 flame HAB, long acquisition time and a preliminary analysis performed on all samples have been deemed  
146 necessary to find the optimal laser irradiance to record high-quality Raman spectra, the existence of which  
147 is acknowledged in our previous work but not explored because of the insufficient signal-to-noise ratio  
148 [46]. About 30 Raman spectra per ROIs are recorded between  $700$  and  $2500 \text{ cm}^{-1}$  for each sample.



## 149 2.5 Analysis of the Raman spectra

150 The first-order Raman spectra of carbonaceous materials are generally characterized by two main  
151 spectral features, labeled D and G bands, at around 1350 and 1600  $\text{cm}^{-1}$ . As detailed in Table 1, an  
152 extensive body of literature has been dedicated to analyzing correlations between chemical and structural  
153 properties of graphene, graphite, highly oriented pyrolytic graphite, carbon films, and soot to some of the  
154 band parameters. [H] is often calculated from the ratio between the slope of the photoluminescence  
155 baseline and the height of the G band [53,54]. Likewise, the degree of graphitization, quantified through  
156 the size of the aromatic domain, has been estimated from the D-to-G band height ratio [11,36,55,56]. The  
157 degrees of disorder and chemical maturity have also been estimated from the shift and broadening of the  
158 G band that seems to depend on the crystallite size [57]. These approaches are relatively simple to  
159 implement but not always optimal for flame-sampled materials. To extract more detailed structural  
160 information, fittings with four [58], five [55,59–61] and up to six [62] different peaks have been discussed  
161 in the literature. However, the peak fitting is a challenging task since the D and G bands are broad,  
162 partially overlap, fold in several contributions, and therefore the exact number and origin of the active  
163 Raman modes are difficult to assess. A common approach to the spectral analysis uses the complete set or  
164 subsets of the peaks listed in Table 1.

165 Following this approach, the Raman spectra obtained in this work are analyzed by curve fitting using  
166 different combinations of the peaks listed in Table 1. The curve fitting is performed with the peak  
167 analyzer tool of OriginPRO 2021 (Levenberg-Marquardt algorithm,  $\chi^2$  tolerance value of  $10^{-6}$  to reach  
168 convergence). The best results ( $R^2 > 0.995$ ) are obtained with six peak fits: D4, D1, D3, G, D2 [59]  
169 expanded to include the peak at 1222  $\text{cm}^{-1}$  [62] here labeled D5 for naming consistency. An example of  
170 the peak fitting is shown in Figure 1. Peaks D4 and D5 are both required to optimally fit the left wing of  
171 the D band, peak D3 is necessary for the otherwise underrepresented local minimum between bands, and  
172 peaks G and D2 are required to reproduce the asymmetrical shape of the G band.

173 In the analysis of Raman spectra of carbonaceous materials, the variability range of the peak centers  
 174 and widths is sometimes fixed or limited for the fitting to reach convergence [55,63]. However, as shown  
 175 in Table 1, some peak assignments are still under debate, therefore limiting the variability range of the  
 176 spectral parameters can ultimately mislead the data interpretation. In particular, the choice of the  
 177 photoluminescence baseline impacts the determination of both the peak centers and widths. In the  
 178 literature, the photoluminescence background is either absent [62], not discussed [46,55,59], or subtracted  
 179 [58,64,65] before fitting. In this work, third-degree polynomial functions are found to be the lowest  
 180 degree polynomials that approximate with high confidence ( $R^2 > 0.995$ ) the rising shape of the  
 181 photoluminescence background in the spectral region 800-2100  $\text{cm}^{-1}$ . The polynomial coefficients and  
 182 constant term are set as free parameters and fitted with the peaks: this approach has the important  
 183 practical advantage that during the fitting it is not necessary to limit peak centers and widths to reach  
 184 convergence.

185

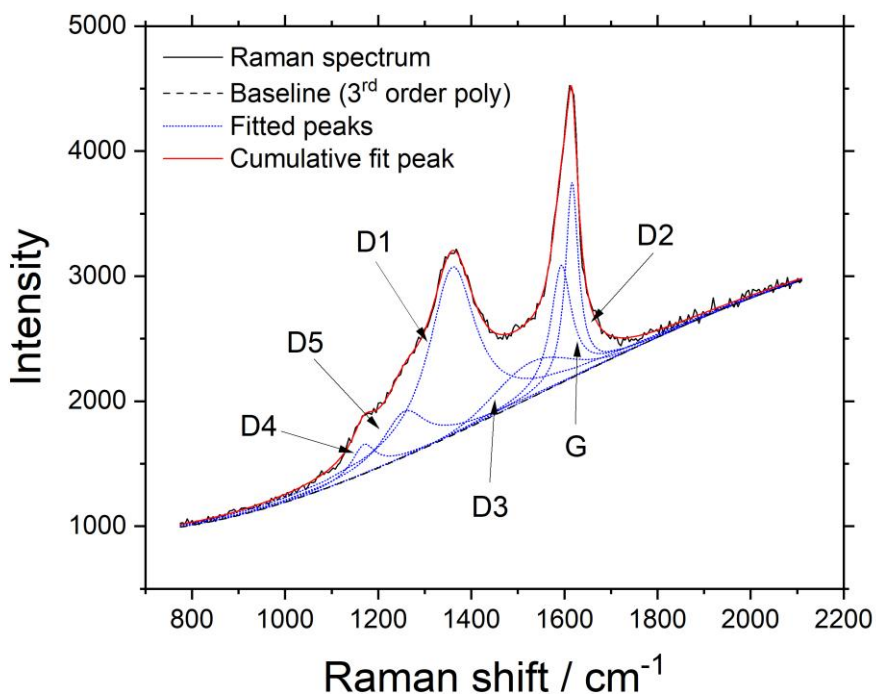
186 **Table 1. Nomenclature and known or proposed assignments** of the peaks used for the spectral analysis of the  
 187 first-order Raman spectra of carbonaceous materials.

Peak	Observed Raman shift / $\text{cm}^{-1}$				Line shape	Bibliographic references
	Sadezky et al. [59]	Minutolo et al. [62]	Parent et al. [55]	Carpentier et al. [64]		
D4	~1200	1176(4)	1180(5)	1175-1190	Lorentz	Assignment under debate. Characteristic of highly disordered materials: polyenes [66], ionic impurities [67], peripheral $\text{sp}^2$ or $\text{sp}^3$ carbon atoms [68].
D5	/	1222(6)	/	1269	Lorentz	Assignment under debate. Finite crystal size or defects [69,70]. Poorly linked polyaromatic units [64]. Already observed in flame-sampled materials [62].
D1	~1350	1340(4)	1350(5)	1337-1372	Lorentz	Certain assignment. $A_{1g}$ ("breathing") mode of graphene only active in case of lattice disturbance (edges due to finite layers, heteroatoms) [71–74].
D3	~1500	1529(4)	1550(5)	1505-1544	Gauss	Assignment under debate. Possibly a convolution of several other modes [55]. Amorphous carbon [66,67,75], finite-size

graphite crystals [76], defects outside graphene layers [77]. A detailed discussion is available [62].

G	~1580	1598(4)	1580(5)	1600	Lorentz	Certain assignment. $E_{2g}$ mode of ideal graphite lattice [71,73].
D2	~1620	1618(4)	1620(5)	1616-1618	Lorentz	Certain assignment. Layers of graphene not directly sandwiched between other layers [55,62,73].

188



189

190 **Figure 1. Raman spectra analysis.** Raman spectrum obtained from a sample collected at 55 mm HAB (514.5 nm  
 191 excitation wavelength,  $1.63 \text{ kW cm}^{-2}$  laser irradiance) and six-peak fitting. The figure shows the acquired spectrum (solid  
 192 black line) and the spectral analysis including the photoluminescence baseline (dashed black line), the peaks D4, D5, D1,  
 193 D3, G and D2 (dotted blue lines) and the cumulative fit curve (solid red line).

194

195 A detailed discussion on the calculation of  $[H]$  from the Raman spectra and comparison with other  
 196 works (SI 8.5) and on the photoluminescence background (SI 8.6) are available in the supporting  
 197 information.

## 198 **2.6 Principal components analysis**

199 Nowadays, the level of complexity of the output of many diagnostics makes it difficult to rely on  
200 intuition or visual analysis to extract trends from raw data. Therefore, statistical tools like multivariate  
201 analysis become increasingly useful to extract any meaningful chemical information from complex  
202 databases.

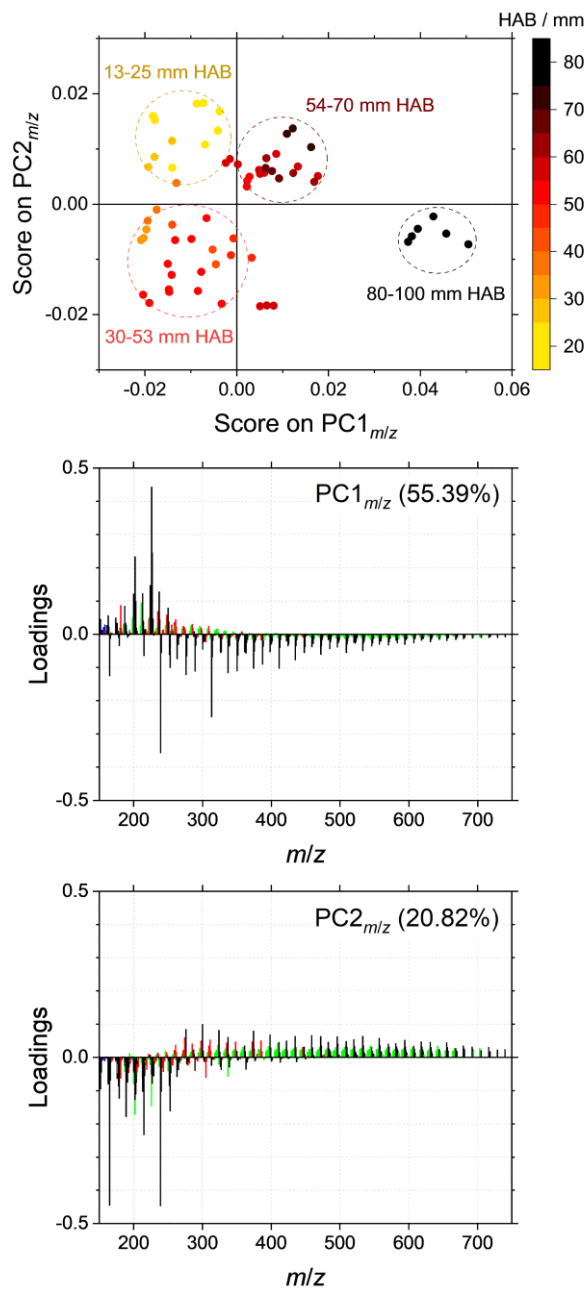
203 Principal component analysis (PCA) is used to reduce the dimensionality of the mass spectra and  
204 Raman spectra databases and to assist the interpretation of the variance [78,79]. The PCA shows the  
205 changes of the variance of a set of observables calculated from a set of variables. The loading plots find  
206 the variables that have the largest effect on each principal component. Therefore, if a principal component  
207 can be linked to a specific physical phenomenon, the PCA indicates the variables upon which this  
208 phenomenon depends. In this work, the  $m/z$  from the ToF-SIMS mass spectra or the spectral parameters  
209 from the peak fitting of the Raman spectra are used as variables, while the data acquisitions on the  
210 sampling zones and various ROIs are used as observables. The additional information on the physical  
211 phenomena is provided by the complementary diagnostics (LII and LIF that map the formation regions of  
212 soot and molecular precursors, and EPR that provides the spin concentration), and by the presence of  
213 visible soot deposits on the analyzed substrates. PCA on non-similar quantities (positions and widths of  
214 the Raman peaks) is performed on the correlation matrix. PCA on similar quantities (ToF-SIMS ion  
215 counts normalized to the total relevant ion count and Raman peak areas normalized to the total area of the  
216 spectrum after removing the photoluminescence background) is performed on the covariance matrix. The  
217 results are then discussed in terms of scores and loadings [35,80,81], with the primary goal of finding  
218 correlations between the chemical composition (ToF-SIMS mass spectra) and the structure (Raman  
219 spectra) of the samples.

220 The four principal components of the PCA on mass spectrometry data (SI 8.4) and on Raman  
221 spectroscopy data (SI 8.7) are shown in the supporting information.

## 222 **3. Results**

### 223 **3.1 The chemical composition of soot**

224 A total of 132 ToF-SIMS mass spectra collected at 21 different HABs are analyzed. The data recorded  
225 on impaction ROIs show the contributions of both soot (only present above the soot inception HAB) and  
226 condensable gas, while the data recorded on the surrounding halo ROIs only show the contribution of  
227 condensable gas. The information extracted from the mass spectra includes the  $m/z$  and the normalized  
228 ion count  $I_n$  of 520 selected peaks. Rather than working with the complete set of detected peaks, scalar  
229 variables are built to represent trends in the mass spectra. To this end, PCA is a particularly useful tool  
230 since the principal components are already defined as linear combinations of the original variables ( $I_n$ ),  
231 and can be related to changes of the variance through the score plots [79]. The results of the PCA on the  
232 complete database of mass spectra are discussed in the exploratory data analysis (SI 8.8). The results of  
233 the PCA on the impaction ROIs are shown in Figure 2. The  $PC2_{m/z}$  against  $PC1_{m/z}$  score plot lays the  
234 foundation for the discussion since  $PC1_{m/z}$  and  $PC2_{m/z}$  represent a significant fraction of the total variance  
235 (76.21%) of the chemical composition. The score plot reveals several data clusters representing samples  
236 having sufficiently different chemical composition to be classified on either  $PC1_{m/z}$  or  $PC2_{m/z}$ . It should be  
237 stressed that the interpretation proposed herein is based on the analysis of  $PC1_{m/z}$  and  $PC2_{m/z}$ , which, while  
238 responsible for the highest contributions, are by no means the only contributors to the variance of the  
239 database.



240

241 **Figure 2. Results of the PCA (covariance matrix) performed on the peak normalized areas extracted from the**  
 242 **impaction ROIs mass spectra.** The figure shows the PC2<sub>m/z</sub> against PC1<sub>m/z</sub> score plot with data cluster attributions (top  
 243 panel) and the corresponding loading plots (middle and bottom panels). The loadings are color-mapped on the assigned  
 244 formula: C<sub>m</sub>H<sub>n</sub><sup>+</sup> (black), C<sub>m</sub>H<sub>n</sub>O<sub>p</sub><sup>+</sup> (red) and unassigned (green).

245

### 246 **3.2 High $m/z$ hydrocarbons (PC1 $_{m/z}$ )**

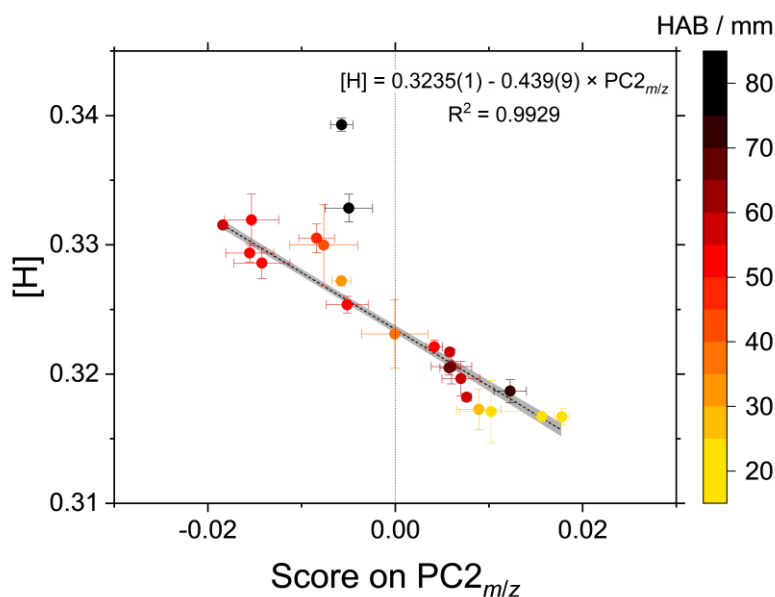
247 On PC1 $_{m/z}$  (55.39% of the total variance explained) three data clusters can be identified as shown in  
248 Figure 2. All mass spectra at 13-53 mm HAB (yellow-orange datapoints) exhibit negative scores on  
249 PC1 $_{m/z}$ . The high dispersion of the datapoints on PC1 $_{m/z}$  indicates that the PCA cannot find statistically  
250 significant differences among the mass spectra of the samples collected in this HAB range. The mass  
251 spectra at 54-70 mm HAB (red-brown datapoints) are closely clustered with low positive scores in PC1 $_{m/z}$ ,  
252 except the mass spectra at 56 mm HAB with close-to-zero negative scores. Finally, the mass spectra at  
253 80-100 mm HAB (black datapoints) exhibit high positive scores in PC1 $_{m/z}$ . The  $m/z$  contributing to PC1 $_{m/z}$   
254 are shown in the corresponding loading plot in Figure 2. A sign inversion of the loadings occurs in the  
255 240-300  $m/z$  range (corresponding to C19-C24 hydrocarbons), which essentially divides the loadings into  
256 two groups: high  $m/z$  ions having high negative loadings, and low  $m/z$  ions having high positive loadings.  
257 The former are almost invariably identified as C $_m$ H $_n^+$  by mass defect analysis and their molecular  
258 formulae are consistent with PAHs or their derivatives, whereas the latter are identified as C $_m$ H $_n^+$ ,  
259 C $_m$ H $_n$ O $_p^+$  and other unassigned ions by mass defect analysis and their molecular formulae are consistent  
260 with PAHs, their derivatives or oxygen-containing hydrocarbons. In the score plot, a sign inversion of the  
261 loadings of PC1 $_{m/z}$  occurs between 53 and 56 mm HAB that calls attention to a change in the chemical  
262 composition of the samples. This change, consisting of the depletion of high  $m/z$  PAHs and their  
263 derivatives in favor of lower  $m/z$  PAHs, their derivatives, and oxygen-containing hydrocarbons, is the first  
264 important information extracted from the analysis of the chemical composition of the samples.

### 265 **3.3 The atomic fraction of hydrogen (PC2 $_{m/z}$ )**

266 On PC2 $_{m/z}$  (20.82% of the variance explained) two data clusters can be identified as shown in Figure 2.  
267 Mass spectra at 30-53 mm HAB (orange-red datapoints) and 80-100 mm HAB (black datapoints) exhibit  
268 negative scores, whereas mass spectra at 13-25 mm HAB (yellow datapoints) and 54-70 mm HAB (brown  
269 datapoints) exhibit positive scores. The  $m/z$  contributing to PC2 $_{m/z}$  are also shown in the corresponding  
270 loading plot in Figure 2. Again, a sign inversion of the loadings occurs approximately in the 240-300  $m/z$

271 range. Here, high  $m/z$  ions have loadings close to zero and therefore only marginally contribute to the  
272 phenomenon represented by  $PC2_{m/z}$ , whereas low  $m/z$  ions having high negative loadings are  
273 predominantly identified as  $C_mH_n^+$ .

274 [H] is linearly correlated to  $PC2_{m/z}$  ( $R^2 = 0.9223$ ) for samples collected up to 70 mm HAB, as shown in  
275 Figure 3. High [H] corresponds to high negative scores on  $PC2_{m/z}$ , i.e. to samples collected at 30-53 mm  
276 and 80-100 mm HAB. As further discussed below, this finding is particularly interesting as it shows that  
277 samples at 30-53 mm HAB have the highest concentration of hydrogen potentially available for chemical  
278 reactivity. Furthermore, the highest negative loadings on  $PC2_{m/z}$  correspond to hydrocarbons in the range  
279 150-260  $m/z$ . Higher  $m/z$  species, being either hydrocarbons, oxygen-containing hydrocarbons or other  
280 unknown species, tend to show significantly lower loadings (see Figure 2) and thus give smaller  
281 contributions to  $PC2_{m/z}$ . Above 80 mm HAB the linear correlation between [H] and  $PC2_{m/z}$  is lost, possibly  
282 because of the oxidation processes becoming dominant as further discussed below.



283  
284 **Figure 3. [H] against  $PC2_{m/z}$ .** The linear regression (black dashed line) and the 95% confidence interval (gray area) do  
285 not include the data collected at 80-100 mm HAB (two isolated black datapoints), for which the correlation is lost.  
286



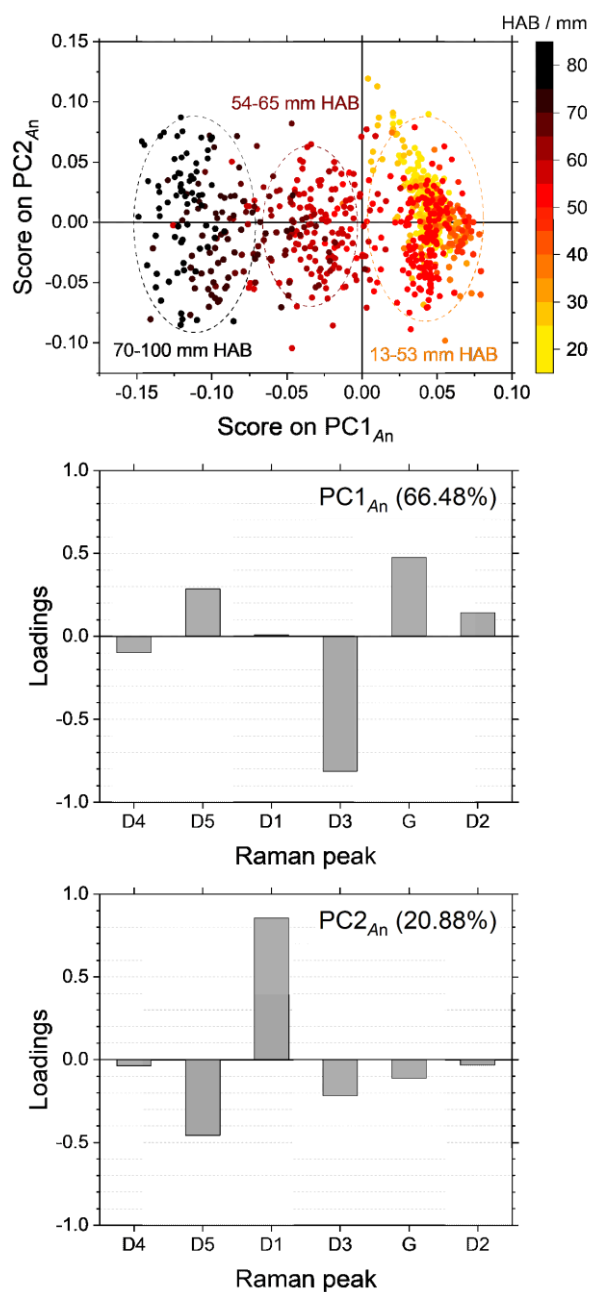
### 287 **3.4 Raman spectroscopy: a challenging interpretation**

288 The first-order feature of the Raman spectra, consisting of the D and G bands in the 800-2100  $\text{cm}^{-1}$   
289 range, is analyzed by peak fitting. Extracting information from the Raman spectra of carbonaceous  
290 materials is no trivial task: the D and G bands are broad and partially overlap, and therefore the exact  
291 number and origin of the active Raman modes are still debated. The approach proposed herein is based on  
292 a six-peak fitting (D4, D5, D1, D3, G, D2) and focuses on finding correlations between the spectral  
293 parameters but avoiding existing empirical relationships that might not be valid for the entire range of the  
294 investigated soot properties, especially for incipient soot.

295 A total of 790 Raman spectra of impaction ROIs collected at 22 different HABs are acquired. The  
296 extracted spectral parameters include: the peak normalized area  $A_n$  defined as  $A_n(X) = A(X)/\sum_i A(X_i)$ ,  
297 where  $A(X)$  is the area of peak X after subtracting the photoluminescence baseline, the peak position  $x_c$   
298 and the width  $w_{\text{FWHM}}$  taken as the full width at half maximum (FWHM). Once again, PCA is used to  
299 reduce the dimensionality and to find statistically significant correlations; the discussion is based on the  
300  $\text{PC2}_{A_n}$  against  $\text{PC1}_{A_n}$  score plot.

301 Figure 4 shows the results of the PCA performed on the  $A_n$  for all impaction ROIs. The scores on  $\text{PC1}_{A_n}$   
302 (66.48% of the variance explained) classify the datapoints in three data clusters based on their sampling  
303 HAB: positive scores at 15-53 mm HAB, low negative scores at 54-65 mm HAB, and high negative  
304 scores at 70-100 mm HAB. These distinct data clusters represent the tendency of  $A_n$  to assume constant  
305 values at 15-53 mm HAB (yellow-red datapoints), then to transition through 54-65 mm HAB (brown  
306 datapoints) to eventually reach different constant values at 70-100 mm HAB (black datapoints). The  
307 loading plot of  $\text{PC1}_{A_n}$  shows that different peaks provide opposing contributions to  $\text{PC1}_{A_n}$ . Peaks D4 and  
308 D3 have negative loadings: in particular, peak D3 has high negative loading, i.e. it contributes extensively  
309 to the phenomenon represented by  $\text{PC1}_{A_n}$ , and  $A_n(\text{D3})$  shows the largest relative difference of all peaks  
310 between 15-53 mm HAB and 70-100 mm HAB. Peaks D5, G and D2 have low positive loadings, hence

311 their contribution to  $PC1_{An}$  opposes that of peaks D4 and D3. Finally, peak D1 has loading close to zero,  
 312 and therefore contributes only marginally to the phenomenon represented by  $PC1_{An}$ .



313  
 314 **Figure 4. Results of the PCA (covariance matrix) performed on the peak normalized areas  $A_n$  extracted from the**  
 315 **impaction ROIs Raman spectra.** The figure shows the  $PC2_{An}$  against  $PC1_{An}$  score plot with data cluster attributions (top  
 316 panel) and the corresponding loading plots (middle and bottom panels).  
 317

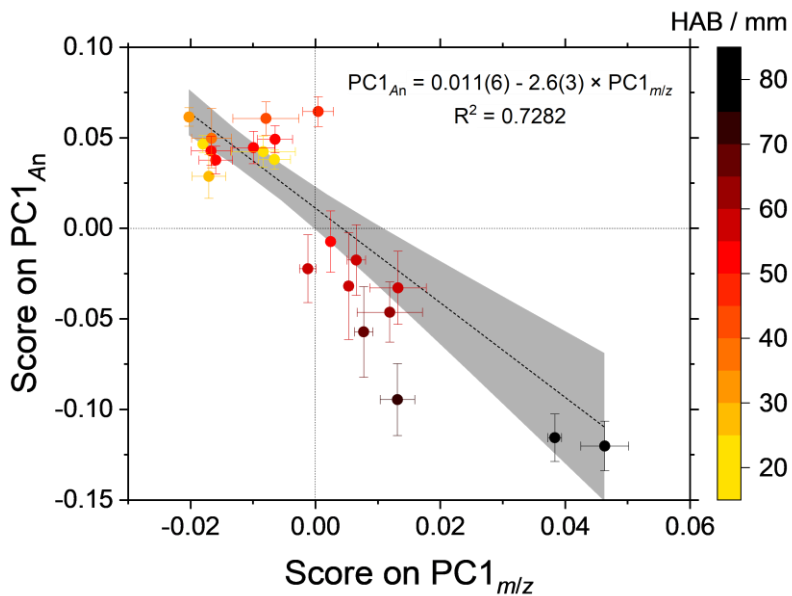
318 The higher-order principal components do not show any appreciable dependence on the HAB or other  
319 identified properties of the samples.

320 The second parameter derived from the fittings,  $x_c$ , is independent of both the flame and sampling  
321 conditions. The data scores overlap in the same region of the score plots and cannot be clearly clustered  
322 (SI 8.7), with the only exception of a small data cluster having high positive scores in the third principal  
323 component that is consequence of a  $\sim 10 \text{ cm}^{-1}$  shift to a higher wavenumber of the D band occurring in  
324 samples collected at 40-45 mm HAB. A similar behavior has already been observed in materials sampled  
325 from premixed flames [11]: there, the authors remark that strains in the lattice or doping from electrical  
326 charges could be at the origin of band shifts in both the D and G bands, and suggest that it could be  
327 evidence of a transition from a planar lattice to the bent crystallites typical of soot nanoparticles.

328 Akin to what has been previously observed for  $A_n$ , the last parameter  $w_{\text{FWHM}}$ , also shows a separation in  
329 three data clusters that represent the tendency of all peaks except D5 to broaden in samples collected at  
330 54-70 mm HAB (SI 8.7). This peak broadening is consistent with the global broadening of the Raman  
331 spectra, with D and G bands spanning over  $1000\text{-}1800 \text{ cm}^{-1}$  in samples collected at 15-53 mm HAB and  
332 over  $900\text{-}1900 \text{ cm}^{-1}$  in those collected at 70-100 mm HAB.

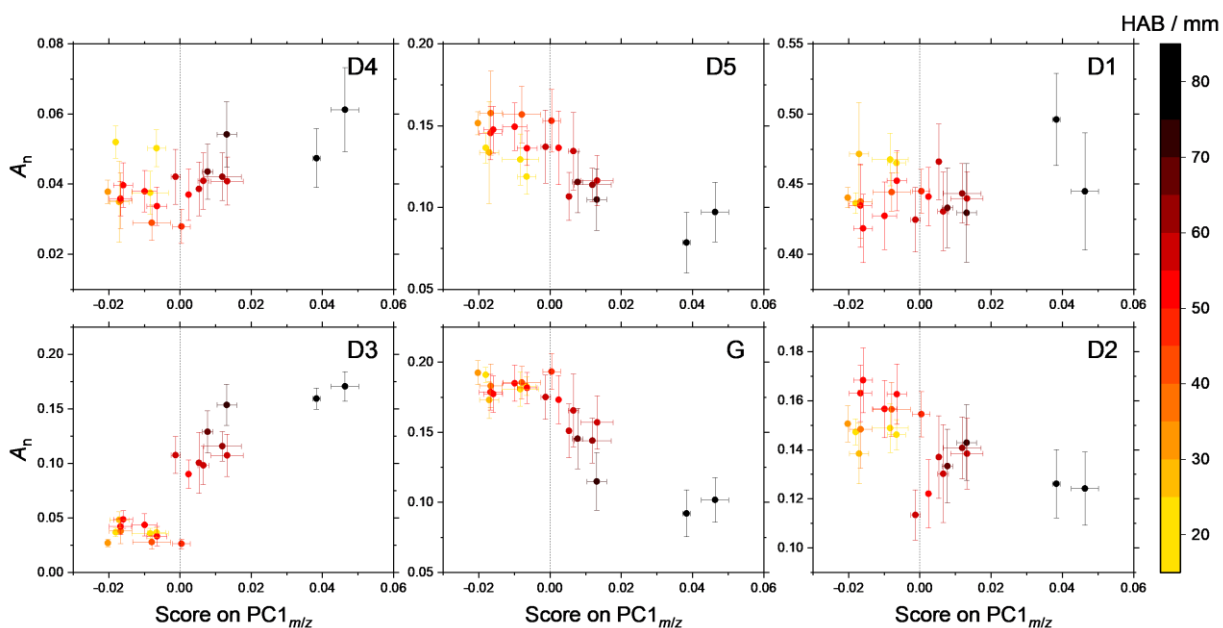
### 333 **3.5 Linking structure and chemical composition**

334 As emerged from the data analysis so far,  $\text{PC1}_{m/z}$  (high  $m/z$  hydrocarbons),  $\text{PC2}_{m/z}$  ([H]) and  $\text{PC1}_{A_n}$   
335 (Raman peaks D5, D3 and G) are convenient choices to represent changes of the chemical composition  
336 and structure of the samples. As shown in Figure 5,  $\text{PC1}_{m/z}$  and  $\text{PC1}_{A_n}$  are correlated: high negative scores  
337 on  $\text{PC1}_{m/z}$  correspond to high positive scores on  $\text{PC1}_{A_n}$  (13-53 mm HAB), low positive scores on  $\text{PC1}_{m/z}$   
338 correspond to low negative scores on  $\text{PC1}_{A_n}$  (54-70 mm HAB), and high positive scores on  $\text{PC1}_{m/z}$   
339 correspond to high negative scores on  $\text{PC1}_{A_n}$  (80-100 mm HAB).



340  
 341 **Figure 5. Linking structure and chemical composition.**  $PC1_{An}$  against  $PC1_{m/z}$  plot. The linear fitting (black dashed line)  
 342 and the 95% confidence interval (gray area) are shown. In this and all following figures, the averages calculated on all the  
 343 available ROIs are compared since it was not possible to perform ToF-SIMS and Raman analyses on the same locations on  
 344 the sample surface.

345  
 346 The sign inversion of  $PC1_{m/z}$ , which occurs approximately in the 240-300  $m/z$  range and corresponds to  
 347 C19-C24 hydrocarbons, represents the depletion of high  $m/z$  hydrocarbons ( $PC1_{m/z} < 0$ ). The Raman  
 348 peaks affected by this change of the chemical composition are identified by comparing the scores on  
 349  $PC1_{m/z}$  to the  $A_n$  of the individual peaks obtained from the curve fitting of the Raman spectra. As shown in  
 350 Figure 6, several behaviors of  $A_n$  against  $PC1_{m/z}$  are identified.



351

352 **Figure 6.  $A_n$  (Raman spectral analysis) against scores on  $PC1_{m/z}$  (ToF-SIMS analysis).**

353

354  $A_n(D4)$  is weakly correlated to  $PC1_{m/z}$ . It is not clear whether a threshold at the sign inversion of  $PC1_{m/z}$   
 355 occurs. While the origin of peak D4 is not yet understood, it has been suggested to be related to the  
 356 presence of polyenes [66], peripheric carbon atoms [59,66,68] or ionic impurities [67]. In any case, peak  
 357 D4 seems to be only weakly affected by the presence of high  $m/z$  hydrocarbons.

358  $A_n(D5)$  is correlated to  $PC1_{m/z}$ , suggesting a dependence on the presence of high  $m/z$  hydrocarbons.  
 359 Although peak D5 has already been observed in flame-sampled materials [62], only little information is  
 360 available on its origin. Peak D5 has been proposed to be activated by the relaxation of the selection rules  
 361 from finite crystal size effects or defects [69,70] or the merging of Raman active modes of poorly linked  
 362 polyaromatic units [64,82].

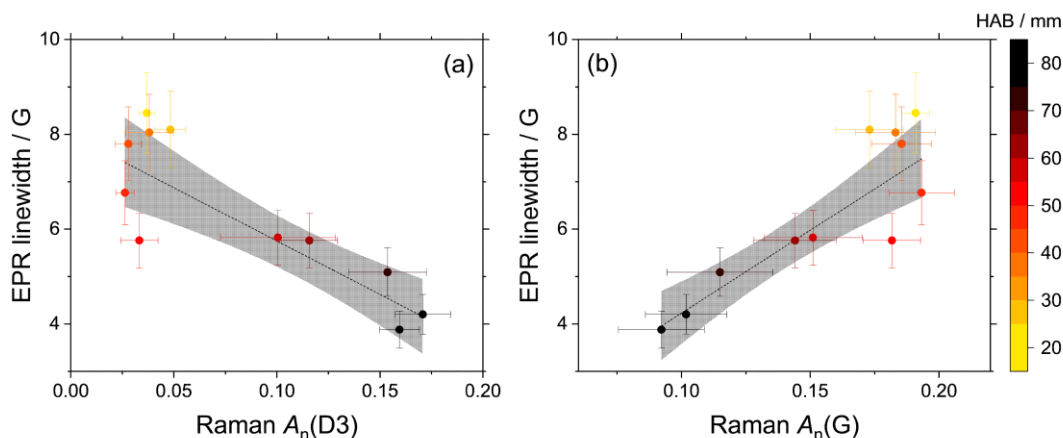
363  $A_n(D1)$  is uncorrelated to  $PC1_{m/z}$ . Peak D1 has been assigned to the  $A_{1g}$  (“breathing”) mode of graphene  
 364 that is only active in case of lattice disturbances like edges or the presence of heteroatoms [71–74,83], and  
 365 has already been established in the literature as a useful marker for mature soot [55,62,84,85]. In this  
 366 work, peak D1 is not found to be an effective marker for the presence of high  $m/z$  hydrocarbons.

367  $A_n(\text{D3})$  is correlated to  $\text{PC1}_{m/z}$ , and furthermore the data clustering already observed in  $\text{PC1}_{A_n}$  is  
368 preserved. In particular, the sharp transition from 13-53 mm HAB (yellow-orange datapoints) to  
369 54-65 mm HAB (red-brown datapoints) corresponds to the sign inversion of  $\text{PC1}_{m/z}$ , i.e. to the depletion  
370 of high  $m/z$  hydrocarbons. The origin of peak D3 is not yet fully understood: in previous works, it has  
371 been attributed to the presence of amorphous carbon [66,67,75], finite-size graphite crystals [76], or  
372 defects outside the graphene layers [77]. Density functional calculations suggest that it might be the  
373 convolution of several Raman active modes [55]. New insights on the origin of peak D3 come from EPR  
374 measurements. Narrow EPR linewidths are characteristic of amorphous carbon or dehydrogenation during  
375 maturation [86]. Figure 7a shows the remarkable correlation between the EPR linewidth of soot samples  
376 collected from the same flame analyzed in this work [48] and the corresponding  $A_n(\text{D3})$  that supports the  
377 attribution of peak D3 to vibrations of amorphous carbon.

378  $A_n(\text{G})$  is correlated to  $\text{PC1}_{m/z}$  with a well-defined threshold behavior.  $A_n(\text{G})$  is constant for negative  
379  $\text{PC1}_{m/z}$  at 13-53 mm HAB, then suddenly decreases at the sign inversion of  $\text{PC1}_{m/z}$ . Peak G has been  
380 unequivocally assigned to the vibration mode  $E_{2g}$  of the ideal graphitic lattice [71,73]. The correlation  
381 between the EPR linewidth and  $A_n(\text{G})$  shown in Figure 7b suggests that the transition to amorphous  
382 carbon is associated with the reduction of the size of the graphitic lattice.

383  $A_n(\text{D2})$  is weakly correlated to  $\text{PC1}_{m/z}$ . Peak D2 has been assigned to isolated graphene layers not  
384 directly sandwiched between other layers [55,62,73].

385 No clear trends emerge when comparing the individual  $A_n$  to  $\text{PC2}_{m/z}$  (SI 8.9).  $A_n(\text{D4})$  shows a weak  
386 correlation to  $\text{PC2}_{m/z}$ , while  $A_n(\text{D5})$ ,  $A_n(\text{D1})$ ,  $A_n(\text{D3})$ ,  $A_n(\text{G})$  and  $A_n(\text{D2})$  are found to be uncorrelated to  
387  $\text{PC2}_{m/z}$ .



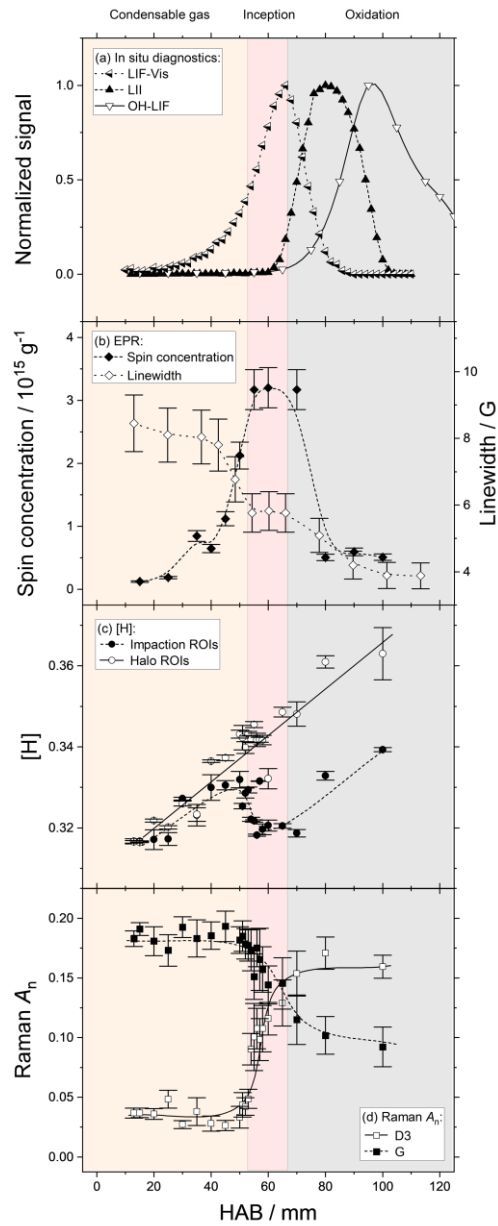
388  
 389 **Figure 7. EPR linewidth and interpretation of Raman spectra.** EPR linewidth against  $A_n(D3)$  (a) and against  $A_n(G)$  (b).  
 390 The linear fitting (black dashed line) and the 95% confidence interval (gray area) are shown. Both correlations are  
 391 statistically significant ( $R^2 > 0.7$ ).  
 392

## 393 4. Discussion

### 394 4.1 Connecting the dots: toward a better understanding of soot inception

395 Figure 8 shows the available data that is found to be dependent on the flame HAB and that includes: (a)  
 396 the normalized in situ profiles of the fluorophores (obtained by laser induced fluorescence, LIF) and the  
 397 laser induced incandescence (LII) signal [50] that is directly proportional to the soot volume fraction; (b)  
 398 the spin concentration of the persistent radicals (obtained by electron paramagnetic resonance, EPR) [48];  
 399 (c) the [H] of the impaction and halo ROIs (obtained by ToF-SIMS, this work); (d) the intensity of the  
 400 vibrations of carbon crystals of finite size and flat graphene-like structures (obtained by Raman  
 401 spectroscopy, this work). This multi-diagnostic approach allows the identification of distinct regimes in  
 402 the flame axis based on differences in the chemical composition, structure and optical properties of the  
 403 condensable gas and of the condensed phase. Information on incipient soot and its molecular precursors is  
 404 then inferred from the comparative analysis.

405



406

407 **Figure 8. Dependence of the investigated quantities on the flame HAB.** The in-situ characterization of the flame  
 408 includes (a) the normalized profiles of the fluorescence induced with 532 nm excitation wavelength (half down left  
 409 triangles [35,50]), the LII signal (solid up triangles [50]), and the OH radicals fluorescence (hollow down triangles [51]).  
 410 The ex-situ characterization of the samples includes: (b) the spin concentration of persistent radicals (solid diamonds  
 411 [48]) (c) the [H] of the impaction (solid rounds) and halo (hollow rounds) ROIs, (d)  $A_n(D3)$  (hollow squares) and  $A_n(G)$   
 412 (solid squares) of the impaction ROIs. All connecting lines are guidelines.

413



414 At 13-30 mm HAB the chemical composition of the condensable gas does not change significantly with  
415 the HAB or the ROI. In this HAB range, high  $m/z$  hydrocarbons are already available (Figure 2). The  
416 mass defect of the identified ions corresponds to or is slightly higher than pericondensed PAHs, but much  
417 lower than the aliphatic and benzene oligomers limits [35,87]. The vast majority of the molecular  
418 formulae assigned by mass defect analysis are consistent with PAHs and PAHs substituted by short  
419 aliphatic chains, and are in good agreement with works that identified in young soot aliphatic molecules  
420 [33,34] and low  $m/z$  aliphatic fragment ions [35].

421 Evidence of change in the flame properties and in the chemistry of the extracted samples begins around  
422 30 mm HAB. First, the induced fluorescence emission progressively shifts toward visible wavelengths  
423 [50]. As previously discussed, evidence has been found that this emission, which was first observed in the  
424 1980s [88,89] and initially attributed to large aromatic molecules [90], might be associated with  
425 long-lived PAH excimers [50,91] or radicals [48] instead. In parallel, the spin concentration of the  
426 persistent radicals increases (Figure 8b). Around 40 mm HAB, the EPR bandwidth (Figure 8b) begins to  
427 decrease and the [H] of the impaction and halo ROIs begins to diverge (Figure 8c).

428 In the impaction ROIs below 53 mm HAB, the intensity of the vibrations attributed to amorphous  
429 carbon and to the ideal graphitic lattice (peaks D3 and G, respectively, Figure 8d) is constant. This lack of  
430 evolution conveys important information: first, it supports the assignment of the ions detected by mass  
431 spectrometry to flat and isolated or weakly bound PAHs. Second, it clearly shows that the structure of the  
432 matter in the condensable gas does not change against the HAB. In this HAB range, no black body-like  
433 emission typical of the matter in the condensed phase is detected in situ in the flame (absence of LII  
434 signal, Figure 8a).

435 At 53-56 mm HAB, several drastic changes occur within a few mm in the ex situ samples that acquire  
436 the character of a discontinuity point. The chemical composition of the impaction ROIs (condensable gas  
437 and condensed phase) and of the halo ROIs (condensable gas only) diverge (Figure 8c). In particular, the  
438 decreasing [H] of the impaction ROIs, not observed at lower HAB or in the halo ROIs, is consistent with  
439 an emerging chemical reactivity compatible with the increasing formation rate of covalent C-C bonds that

440 supports the occurrence of cross-linking or dimerization as discussed in our previous work [46]. In the  
441 impaction ROIs, the relative contribution of high  $m/z$  hydrocarbons decreases in favor of lower  $m/z$   
442 hydrocarbons and oxygen-containing hydrocarbons ( $PC1_{m/z}$  loadings sign inversion, Figure 2). This  
443 depletion is consistent with the recently observed accumulation of PAHs on soot particles [92], and  
444 strongly suggests that incipient soot acts as sinks for high  $m/z$  hydrocarbons. The structure of the species  
445 in the impaction ROIs undergoes significant changes within the narrow 53-54 mm HAB range. First, the  
446 intensity of the vibrations of the graphitic lattice, that are constant up to 53 mm HAB, begin to decrease  
447 (Raman peak G, Figure 8c): a similar phenomenon has already been observed and suggested to be an  
448 indicator of the formation of curved structures as opposed to the flat aromatic species more abundant  
449 before soot inception [37,56]. At the same time, the intensity of the vibrations attributed to amorphous  
450 carbon suddenly rises (Raman peak D3, Figure 8c). The spin concentration and the fluorescence emission  
451 reach their maximum at 55-70 mm HAB (Figure 8b) and 65-70 mm HAB (LIF induced with 532 nm  
452 excitation wavelength, Figure 8a), respectively. The EPR bandwidth (Figure 8b) remains approximately  
453 constant, while black body-like emission of matter in the condensed phase is initially detected at 60 mm  
454 HAB (in situ LII signals with  $SNR \geq 3$ , Figure 8a).

455 At 70-100 mm HAB the soot volume fraction reaches its maximum while the concentration of  
456 fluorophores detected in situ decreases against HAB (LII and LIF profiles, respectively, Figure 8a). High  
457  $m/z$  hydrocarbons are depleted (Figure 2). The intensity of the vibrations of the graphitic lattice further  
458 decreases, while the intensity of the vibrations attributed to amorphous carbon reaches its maximum  
459 (Raman peaks G and D3, respectively, Figure 8b). The spin concentration reaches a minimum, and the  
460 EPR bandwidth further decreases (Figure 8b). All these changes are already well documented in the  
461 literature [1,3,4] and represent the transition from young to mature and (partially) oxidized soot. This  
462 second transition occurs in a broader HAB range than the former, and involves more clearly the structure  
463 rather than the chemical composition of the sampled materials (no sign inversion of  $PC1_{m/z}$ , Figure 2). The  
464 oxidation processes becoming dominant (rise of the concentration of OH radicals that begins around  
465 65 mm HAB) reasonably explains the depletion of the high  $m/z$  hydrocarbons (high scores in  $PC1_{m/z}$ ,

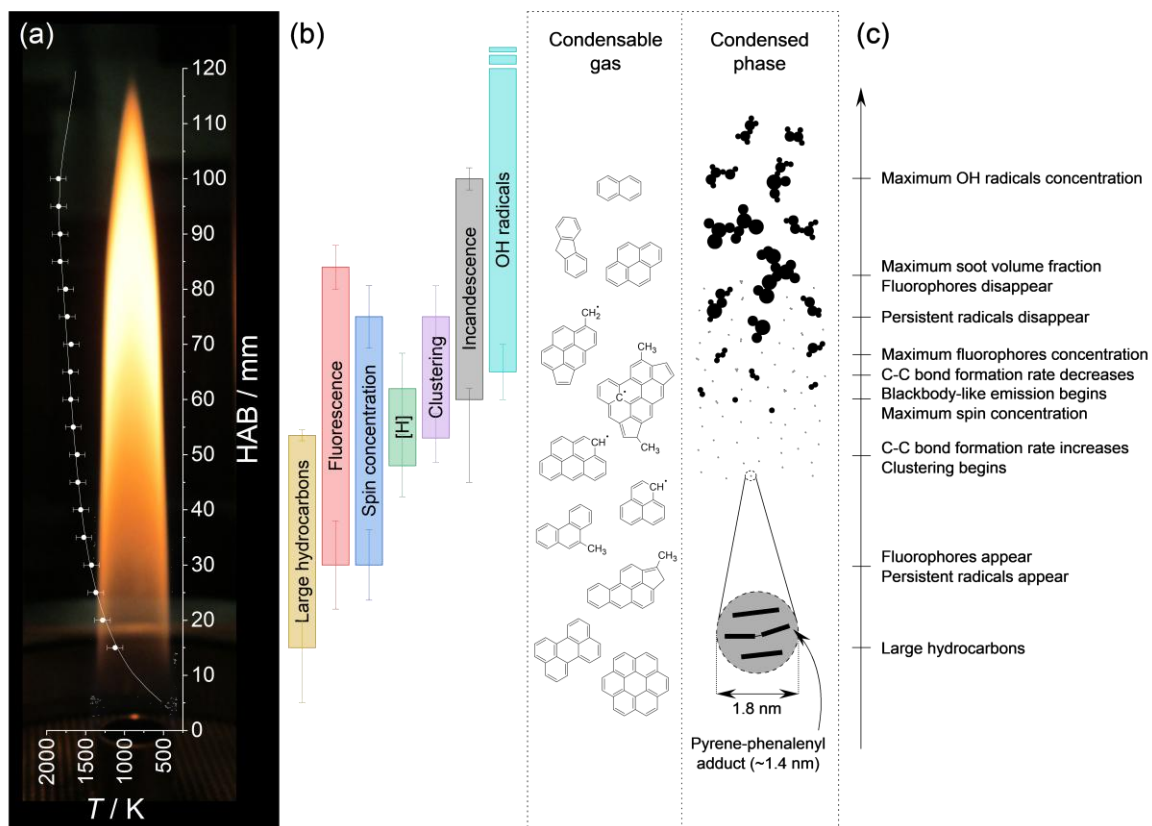
466 Figure 2), but also the disappearance of the mature soot particles that are almost entirely oxidized higher  
467 in the flame (the diffusion flame is non-smoking). The transition to a regime where the dominating  
468 mechanism is oxidation could also explain the loss of linearity in the correlation between [H] and  $PC2_{m/z}$   
469 previously discussed (see section 3.3), as the hydrocarbons found in this region likely have a more diverse  
470 nature than the PAHs generated only by molecular growth processes like the HACA.

#### 471 **4.2 A simple phenomenological model of soot inception**

472 An overview of the experimental findings is provided in Figure 9. Based on purely phenomenological  
473 considerations, the hypothesis is made that in this diffusion flame the reactive species responsible for soot  
474 inception are formed from the pool of the PAHs and substituted PAHs already available at low HAB. As  
475 the flame temperature increases, the concentration of reactive species also increases until it can sustain the  
476 formation of adducts. In the flame axis, a critical point is reached at 53-54 mm HAB (1600-1650 K [51]),  
477 where the increased formation rate of C-C bonds results in a global decrease of [H], immediately  
478 followed by the detection of graphite-like crystals in the condensed phase ex situ, and slightly higher at 60  
479 mm HAB (~1700 K) by in situ black body-like emission.

480 A possibility that should be considered is that the chain of events leading to soot inception begins  
481 before the black body-like emission of soot is detected. In this context, the lower limit of detection of the  
482 LII diagnostic becomes a key point for the interpretation of all experimental data. In this work, the first  
483 changes in the chemical composition and structure of the samples consistent with a phase transition occur  
484 6-7 mm lower than the first black body-like emission attributed to particles in the condensed phase. This  
485 discrepancy cannot be accounted for even when including the uncertainty attributed to the sampling  
486 process ( $\pm 2$  mm). Based on the literature reviewed so far, there is consensus that incepting soot particles  
487 have different physical-chemical properties than fully formed primary soot particles, and in particular  
488 their absorption function  $E(m)$  is significantly lower [28,29]. Therefore, the black body-like emission is  
489 detectable only when the particle concentration in the flame becomes sufficiently high, or alternatively  
490 when coagulation and surface growth have already resulted in an increased  $E(m)$ . These two scenarios are

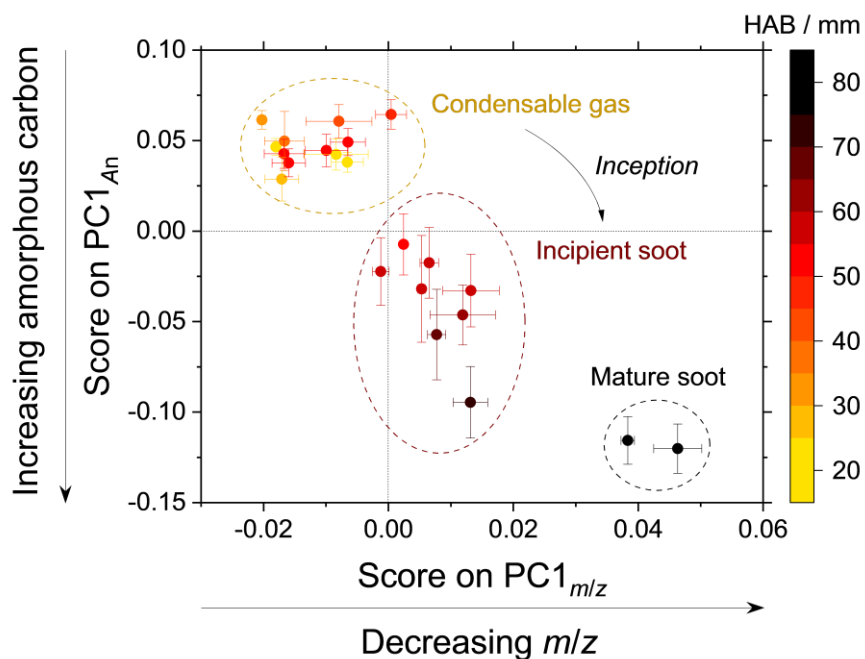
491 not mutually exclusive and are both consistent with a shifted particle detection by LII on the axial profile  
 492 of the flame.



493  
 494  
 495 **Figure 9. Phenomenological scenario for soot inception.** (a) flame picture with overlaid HAB scale and temperature  
 496 profile. (b) Significant HAB ranges: large hydrocarbons (ToF-SIMS on the impaction ROIs, yellow), fluorophores (LIF at  
 497 532 nm excitation wavelength, red), spin concentration (EPR, blue), slope inversion of [H] (green), clustering (changes of  
 498 the D3 and G Raman peaks, purple), black body-like emission (LII, gray), and OH radicals (LIF-OH, cyan). The error bars of  
 499 the quantities obtained from ex-situ diagnostics (EPR, ToF-SIMS and Raman) include the shift introduced with the  
 500 sampling uncertainty (estimated to  $\pm 2$  mm from the change in the flame luminosity and propagated with a Taylor  
 501 expansion). (c) summary of the experimental observation. The depicted soot particles are to scale (2 nm diameter  
 502 incipient soot particles, 5-15 nm diameter primary particles, ~50 nm gyration diameter aggregates). The size of the  
 503 depicted adducts is calculated from aromatic C-C and C-H bond distances.  
 504

505 With this uncertainty in mind, it is interesting to notice that the spin concentration of the persistent  
506 radicals reaches its maximum immediately before the black body-like emission attributed to particles in  
507 the condensed phase is first detected, and begins to decrease when the OH radicals appear and the soot  
508 volume fraction reaches its maximum (Figure 8). These correspondences strongly suggest that the  
509 detected persistent radicals are closely related to the reactive species responsible for soot inception: when  
510 the reactive medium is extracted from the flame and deposited on a solid substrate during sampling, the  
511 surviving reactive species likely transform into the stable products detected by the ex situ diagnostics,  
512 including the persistent radicals detected by EPR. However, a trace is clearly left in the samples as the  
513 spin concentration peaks shortly before the black body-like emission attributed to soot particles is first  
514 detected. In addition, the spin concentration is linearly correlated to the induced fluorescence at 532 nm  
515 [48], i.e. the reactive species that generate the persistent radicals and the fluorophores may share a  
516 common origin. The induced fluorescence [35,50,91] and recent works on the characterization of the  
517 persistent radicals [47,48,93] suggest important contributions from resonance-stabilized radicals of PAHs  
518 substituted by short aliphatic chains. The availability of radical PAHs substituted with side chains might  
519 contribute to further stabilize any multi-layered structure formed via interplanar covalent bonds in  
520 addition to the weaker stacking interactions that are known to be insufficient to hold together clusters of  
521 small PAHs at the flame temperature [94]. This hypothesis is additionally supported by the correlation  
522 between the EPR linewidth and the intensity of the vibration of mode  $E_{2g}$  of the ideal graphitic lattice  
523 found in this work. The decreasing intensity of the vibration of mode  $E_{2g}$  (Figure 7b) and the  
524 disappearance of large PAHs (Figure 2) suggest that the initial formation of amorphous carbon is  
525 associated with the reduction of the size of the aromatic domains. This decreasing intensity of the  
526 vibration cannot be a consequence of the increasing number of lattice defects as the intensity of the  
527 vibration of mode  $A_{1g}$  of graphene is not correlated to the soot inception process (peak D1, see Figure 6).  
528 Therefore, it must be concluded that the observed reduction of the size of the aromatic domains is caused  
529 by the formation of curved and/or multi-layer structures.

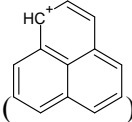
530 Higher in the flame, around 70-75 mm HAB, this equilibrium is upset. The slope of [H] changes its  
 531 sign again, indicating that the formation rate of C-C bonds decreases, the emission of the fluorophores  
 532 and the spin concentration of the persistent radicals are reduced to roughly one tenth of their peak value.  
 533 All this information indicates that soot inception reaches an abrupt halt shortly before the maximum soot  
 534 volume fraction is detected. As already noticed above, this second series of changes corresponds  
 535 remarkably well to the rise of the concentration of OH radicals. Therefore, it can be inferred that the OH  
 536 radicals first inactivate the most reactive species in the flame, which subsequently slows down the  
 537 formation rate of C-C bonds, and finally stabilizes the structure of the particles to that of mature soot. In  
 538 particular, soot sampled above the maximum soot volume fraction show no visual trace of the brown  
 539 organic matter that is prominent in the samples collected at lower HAB [48].

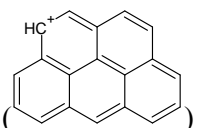


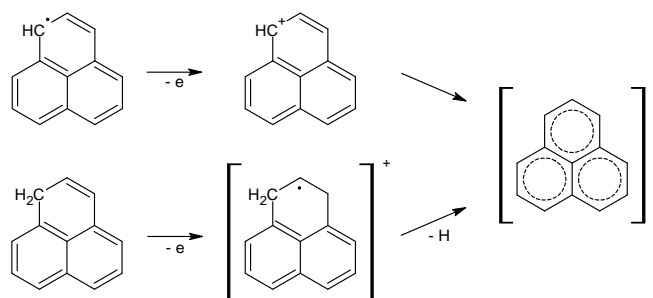
540  
 541 **Figure 10. Soot inception identified by the PCA (Figure 5 revisited).** PC1<sub>An</sub> against PC1<sub>m/z</sub> plot emphasizing the  
 542 existence of three data clusters. Increasing scores on PC1<sub>m/z</sub> represent the increasing relative contribution of low *m/z*  
 543 PAHs and their derivatives (section 3.1), while decreasing scores on PC1<sub>An</sub> represent the increasing relative contribution  
 544 of amorphous carbon (section 3.4). Notice how the data cluster assigned to the incipient soot stands out from the other  
 545 two data clusters.  
 546

547 In light of this discussion, the cross-comparison of the analysis of the chemical composition and  
548 structure of soot becomes an effective way to represent soot inception. Figure 10 shows the  $PC1_{An}$  against  
549  $PC1_{m/z}$  plot, already discussed in section 3.5, with three highlighted data clusters representing different  
550 regimes separated by discontinuities and assigned to condensable gas, incipient soot and mature soot.  
551 This representation well summarizes the main information extracted from this study, and in particular  
552 highlights the existence of incipient soot as a distinct regime with chemical composition and structure  
553 significantly different than either the condensable gas and the mature soot.

554 In our previous work, the potential link between the formation of dimers of small PAHs and soot  
555 inception has been discussed at length [46]. As a final remark, we would like to bring attention to the  
556 cations that mark the beginning and the maximum of the negative  $PC1_{m/z}$  loadings distribution in the  
557 analysis of mass spectrometry data, and specifically to the first cation of the distribution  $C_{13}H_9^+$   
558 (165.070 u) and to the cation with the largest variability in the sequence of high  $m/z$  hydrocarbons  $C_{19}H_{11}^+$

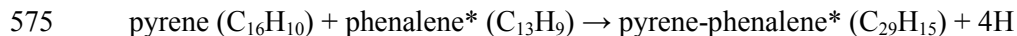
559 (239.086 u). Among the possible isomers, the cations of 1H-phenalene () and

560 6H-benzo[*cd*]pyrene () are particularly interesting as they have attracted considerable  
561 interest in theoretical chemistry for their ability to form relatively stable  $\pi$  dimers [95,96]. On the one  
562 hand, care must be taken when interpreting ex situ mass spectrometry data. Benzenoid PAHs with an odd  
563 number of carbon atoms contain a  $CH_2$  group that can undergo post-ionization hydrogen elimination to  
564 form the same cations as resonance-stabilized radicals as shown below for the case of  
565 phenalene/phenalenyl:



566

567 Therefore, it can be argued that the secondary ions detected ex situ mostly derive from stable PAHs  
 568 rather than reactive radicals since the latter are less likely to survive the sampling process. On the other  
 569 hand, the very existence of a maximum of the spin concentration before the inception zone is clear  
 570 evidence that at least part of the information on the reactive radicals is preserved for a long time after the  
 571 sampling. Within the limits imposed by this interpretation, the intermediate species detected at the very  
 572 beginning of the soot inception zone in our previous work [46] could be the stable products deriving from  
 573 the reactive radicals in the flame. For instance, reactions reminiscent of the formation of Frenklach's  
 574 E-bridges [2] or Selvakumar's  $\pi$ -radicals localization [97] like:



576 would result in adducts capable of forming cations consistent with the observed  $m/z$ . The characteristic  
 577 size of the adducts, calculated from the aromatic bond length of PAHs in the considered mass range and  
 578 shown in scale in Figure 9, is 0.8-1.5 nm, in reasonably good agreement with the estimated size of the  
 579 aromatic domains in this flame [46]. Additionally, similar reactions would explain the observed decrease  
 580 of [H], and being resonance-stabilized, the adducts could be sufficiently stable to survive the sampling  
 581 and be detected ex situ.

## 582 5. Conclusions

583 In this work, the chemical composition and the structure of incipient soot generated in a co-flow  
 584 laminar diffusion flame of methane are investigated with a multi-diagnostic approach. Principal  
 585 component analysis is used to determine the physical variables involved in soot inception, and to link  
 586 them to soot inception, growth and oxidation.



587 The main finding of this work relies on the comparative analysis of the chemical composition (by  
588 secondary ion mass spectrometry) and the structure (by Raman spectroscopy) of incipient soot of samples  
589 extracted from the flame. The results are discussed in light of the information obtained from  
590 complementary diagnostics that include the spin concentration of the extracted samples (by electron  
591 paramagnetic resonance), and the in-flame distribution of the soot volume fraction (by laser induced  
592 incandescence) and of different classes of fluorophores (by laser induced fluorescence). The comparative  
593 analysis shows compelling evidence of the existence of an intermediate state of the matter extracted from  
594 the flame, attributed to incipient soot, having significantly different chemical composition and structure  
595 than the condensable gas and the mature soot. The appearance of this intermediate state occurs suddenly  
596 shortly before the in situ detection of soot particles by laser induced incandescence in the axial direction  
597 of the flame.

598 In terms of chemical composition, the atomic percentage of hydrogen [H] of the intermediate state  
599 shows a slope inversion that suggests the existence of an emerging reactivity absent in the condensable  
600 gas. Based on our past investigation [46], this reactivity is attributed to an increased formation rate of C-C  
601 bonds associated with the formation of incipient soot. The candidate reactive species are identified as  
602 C<sub>12</sub>–C<sub>20</sub> CmH<sub>n</sub><sup>+</sup> hydrocarbons. In addition, the change of slope of [H] corresponds remarkably well to  
603 the maximum of the spin concentration detected by electron paramagnetic resonance, which suggests that  
604 some of the reactive species are radicals.

605 In terms of structure, the physical phenomena linked to the appearance of the intermediate state are the  
606 appearance of amorphous carbon and the progressive disappearance of large and flat aromatic structures,  
607 while the overall number of lattice defects is unaffected.

## 608 **6. Acknowledgments**

609 The authors would like to thank Dr. Edouard Capoen for his invaluable support in the preparation of the  
610 deposition substrates. The authors would also like to acknowledge the contribution of the *Centre d'*  
611 *Etudes et de Recherches Lasers et Applications* (CERLA) platform for the materials and equipment.

612 Financial support for this work was provided by the French *Agence de la Transition Ecologique*  
613 (ADEME).

## 614 7. Bibliography

- 615 [1] Martin JW, Salamanca M, Kraft M. Soot inception: carbonaceous nanoparticle formation in flames.  
616 *Prog Energy Combust Sci* 2022;88:100956. <https://doi.org/10.1016/j.pecs.2021.100956>.
- 617 [2] Frenklach M. Reaction mechanism of soot formation in flames. *Phys Chem Chem Phys*  
618 2002;4:2028–37. <https://doi.org/10.1039/B110045A>.
- 619 [3] D’Anna A. Combustion-formed nanoparticles. *Proc Combust Inst* 2009;32:593–613.  
620 <https://doi.org/10.1016/j.proci.2008.09.005>.
- 621 [4] Wang H. Formation of nascent soot and other condensed-phase materials in flames. *Proc Combust*  
622 *Inst* 2011;33:41–67. <https://doi.org/10.1016/j.proci.2010.09.009>.
- 623 [5] Desgroux P, Mercier X, Thomson KA. Study of the formation of soot and its precursors in flames  
624 using optical diagnostics. *Proc Combust Inst* 2013;34:1713–38.  
625 <https://doi.org/10.1016/j.proci.2012.09.004>.
- 626 [6] Frenklach M, Mebel AM. On the mechanism of soot nucleation. *Phys Chem Chem Phys*  
627 2020;22:5314–31. <https://doi.org/10.1039/D0CP00116C>.
- 628 [7] Michelsen HA, Colket MB, Bengtsson P-E, D’Anna A, Desgroux P, Haynes BS, et al. A review of  
629 terminology used to describe soot formation and evolution under combustion and pyrolytic  
630 conditions. *ACS Nano* 2020;14:12470–90. <https://doi.org/10.1021/acsnano.0c06226>.
- 631 [8] Alfè M, Apicella B, Barbella R, Rouzaud J-N, Tregrossi A, Ciajolo A. Structure–property  
632 relationship in nanostructures of young and mature soot in premixed flames. *Proc Combust Inst*  
633 2009;32:697–704. <https://doi.org/10.1016/j.proci.2008.06.193>.
- 634 [9] Kholghy MR, Veshkini A, Thomson MJ. The core–shell internal nanostructure of soot – A criterion  
635 to model soot maturity. *Carbon* 2016;100:508–36. <https://doi.org/10.1016/j.carbon.2016.01.022>.
- 636 [10] Sgro LA, Barone AC, Commodo M, D’Alessio A, De Filippo A, Lanzuolo G, et al. Measurement of  
637 nanoparticles of organic carbon in non-sooting flame conditions. *Proc Combust Inst* 2009;32:689–  
638 96. <https://doi.org/10.1016/j.proci.2008.06.216>.
- 639 [11] Commodo M, De Falco G, Bruno A, Borriello C, Minutolo P, D’Anna A. Physicochemical  
640 evolution of nascent soot particles in a laminar premixed flame: from nucleation to early growth.  
641 *Combust Flame* 2015;162:3854–63. <https://doi.org/10.1016/j.combustflame.2015.07.022>.
- 642 [12] Moallemi A, Kazemimanesh M, Kostiuk LW, Olfert JS. The effect of sodium chloride on the  
643 nanoparticles observed in a laminar methane diffusion flame. *Combust Flame* 2018;188:273–83.  
644 <https://doi.org/10.1016/j.combustflame.2017.10.009>.
- 645 [13] Totton TS, Chakrabarti D, Misquitta AJ, Sander M, Wales DJ, Kraft M. Modelling the internal  
646 structure of nascent soot particles. *Combust Flame* 2010;157:909–14.  
647 <https://doi.org/10.1016/j.combustflame.2009.11.013>.
- 648 [14] Teini PD, Karwat DMA, Atreya A. Observations of nascent soot: molecular deposition and particle  
649 morphology. *Combust Flame* 2011;158:2045–55.  
650 <https://doi.org/10.1016/j.combustflame.2011.03.005>.
- 651 [15] Botero ML, Sheng Y, Akroyd J, Martin J, Dreyer JAH, Yang W, et al. Internal structure of soot  
652 particles in a diffusion flame. *Carbon* 2019;141:635–42.  
653 <https://doi.org/10.1016/j.carbon.2018.09.063>.
- 654 [16] Ishiguro T, Takatori Y, Akihama K. Microstructure of diesel soot particles probed by electron  
655 microscopy: first observation of inner core and outer shell. *Combust Flame* 1997;108:231–4.  
656 [https://doi.org/10.1016/S0010-2180\(96\)00206-4](https://doi.org/10.1016/S0010-2180(96)00206-4).

- 657 [17] D'Alessio A, Barone AC, Cau R, D'Anna A, Minutolo P. Surface deposition and coagulation  
658 efficiency of combustion generated nanoparticles in the size range from 1 to 10nm. *Proc Combust*  
659 *Inst* 2005;30:2595–603. <https://doi.org/10.1016/j.proci.2004.08.267>.
- 660 [18] Hou D, Zong D, Lindberg CS, Kraft M, You X. On the coagulation efficiency of carbonaceous  
661 nanoparticles. *J Aerosol Sci* 2020;140:105478. <https://doi.org/10.1016/j.jaerosci.2019.105478>.
- 662 [19] Huo Z, Cleary MJ, Sirignano M, Masri AR. A sectional soot formation kinetics scheme with a new  
663 model for coagulation efficiency. *Combust Flame* 2021;230:111444.  
664 <https://doi.org/10.1016/j.combustflame.2021.111444>.
- 665 [20] De Falco G, Picca F, Commodo M, Minutolo P. Probing soot structure and electronic properties by  
666 optical spectroscopy. *Fuel* 2020;259:116244. <https://doi.org/10.1016/j.fuel.2019.116244>.
- 667 [21] Zhao B, Yang Z, Johnston MV, Wang H, Wexler AS, Balthasar M, et al. Measurement and  
668 numerical simulation of soot particle size distribution functions in a laminar premixed ethylene-  
669 oxygen-argon flame. *Combust Flame* 2003;133:173–88. [https://doi.org/10.1016/S0010-2180\(02\)00574-6](https://doi.org/10.1016/S0010-2180(02)00574-6).
- 670 [22] Abid AD, Tolmachoff ED, Phares DJ, Wang H, Liu Y, Laskin A. Size distribution and morphology  
671 of nascent soot in premixed ethylene flames with and without benzene doping. *Proc Combust Inst*  
672 2009;32:681–8. <https://doi.org/10.1016/j.proci.2008.07.023>.
- 673 [23] Carbone F, Moslih S, Gomez A. Probing gas-to-particle transition in a moderately sooting  
674 atmospheric pressure ethylene/air laminar premixed flame. Part II: Molecular clusters and nascent  
675 soot particle size distributions. *Combust Flame* 2017;181:329–41.  
676 <https://doi.org/10.1016/j.combustflame.2017.02.021>.
- 677 [24] Shariatmadar H, Aleiferis PG, Lindstedt RP. Particle size distributions in turbulent premixed  
678 ethylene flames crossing the soot inception limit. *Combust Flame* 2022;243:111978.  
679 <https://doi.org/10.1016/j.combustflame.2021.111978>.
- 680 [25] Michelsen HA. Effects of maturity and temperature on soot density and specific heat. *Proc Combust*  
681 *Inst* 2021;38:1197–205. <https://doi.org/10.1016/j.proci.2020.06.383>.
- 682 [26] Betrancourt C, Mercier X, Liu F, Desgroux P. Quantitative measurement of volume fraction profiles  
683 of soot of different maturities in premixed flames by extinction-calibrated laser-induced  
684 incandescence. *Appl Phys B* 2019;125:16. <https://doi.org/10.1007/s00340-018-7127-2>.
- 685 [27] Kelesidis GA, Pratsinis SE. Soot light absorption and refractive index during agglomeration and  
686 surface growth. *Proc Combust Inst* 2019;37:1177–84. <https://doi.org/10.1016/j.proci.2018.08.025>.
- 687 [28] Yon J, Cruz JJ, Escudero F, Morán J, Liu F, Fuentes A. Revealing soot maturity based on multi-  
688 wavelength absorption/emission measurements in laminar axisymmetric coflow ethylene diffusion  
689 flames. *Combust Flame* 2021;227:147–61. <https://doi.org/10.1016/j.combustflame.2020.12.049>.
- 690 [29] Minutolo P, Commodo M, D'Anna A. Optical properties of incipient soot. *Proc Combust Inst*  
691 2023;39:1129–38. <https://doi.org/10.1016/j.proci.2022.09.019>.
- 692 [30] Mouton T, Mercier X, Wartel M, Lamoureux N, Desgroux P. Laser-induced incandescence  
693 technique to identify soot nucleation and very small particles in low-pressure methane flames. *Appl*  
694 *Phys B* 2013;112:369–79. <https://doi.org/10.1007/s00340-013-5446-x>.
- 695 [31] Betrancourt C, Liu F, Desgroux P, Mercier X, Faccinnetto A, Salamanca M, et al. Investigation of the  
696 size of the incandescent incipient soot particles in premixed sooting and nucleation flames of n-  
697 butane using LII, HIM, and 1 nm-SMPS. *Aerosol Sci Technol* 2017;51:916–35.  
698 <https://doi.org/10.1080/02786826.2017.1325440>.
- 699 [32] Carbone F, Canagaratna MR, Lambe AT, Jayne JT, Worsnop DR, Gomez A. Detection of weakly  
700 bound clusters in incipiently sooting flames via ion seeded dilution and collision charging for (API-  
701 TOF) mass spectrometry analysis. *Fuel* 2021;289:119820.  
702 <https://doi.org/10.1016/j.fuel.2020.119820>.
- 703 [33] Cain JP, Camacho J, Phares DJ, Wang H, Laskin A. Evidence of aliphatics in nascent soot particles  
704 in premixed ethylene flames. *Proc Combust Inst* 2011;33:533–40.  
705 <https://doi.org/10.1016/j.proci.2010.06.164>.
- 706

- 707 [34] Cain J, Laskin A, Kholghy MR, Thomson MJ, Wang H. Molecular characterization of organic  
708 content of soot along the centerline of a coflow diffusion flame. *Phys Chem Chem Phys*  
709 2014;16:25862–75. <https://doi.org/10.1039/C4CP03330B>.
- 710 [35] Irimiea C, Faccinnetto A, Mercier X, Ortega I-K, Nuns N, Therssen E, et al. Unveiling trends in soot  
711 nucleation and growth: When secondary ion mass spectrometry meets statistical analysis. *Carbon*  
712 2019;144:815–30. <https://doi.org/10.1016/j.carbon.2018.12.015>.
- 713 [36] Schulz F, Commodo M, Kaiser K, De Falco G, Minutolo P, Meyer G, et al. Insights into incipient  
714 soot formation by atomic force microscopy. *Proc Combust Inst* 2018;37:885–92.  
715 <https://doi.org/10.1016/j.proci.2018.06.100>.
- 716 [37] Commodo M, Kaiser K, De Falco G, Minutolo P, Schulz F, D’Anna A, et al. On the early stages of  
717 soot formation. Molecular structure elucidation by high-resolution atomic force microscopy.  
718 *Combust Flame* 2019;205:154–64. <https://doi.org/10.1016/j.combustflame.2019.03.042>.
- 719 [38] Vander Wal RL, Tomasek AJ. Soot nanostructure: dependence upon synthesis conditions. *Combust*  
720 *Flame* 2004;136:129–40. <https://doi.org/10.1016/j.combustflame.2003.09.008>.
- 721 [39] Vander Wal RL, Yezerets A, Currier NW, Kim DH, Wang CM. HRTEM Study of diesel soot  
722 collected from diesel particulate filters. *Carbon* 2007;45:70–7.  
723 <https://doi.org/10.1016/j.carbon.2006.08.005>.
- 724 [40] Eaves NA, Dworkin SB, Thomson MJ. The importance of reversibility in modeling soot nucleation  
725 and condensation processes. *Proc Combust Inst* 2015;35:1787–94.  
726 <https://doi.org/10.1016/j.proci.2014.05.036>.
- 727 [41] Camacho J, Tao Y, Wang H. Kinetics of nascent soot oxidation by molecular oxygen in a flow  
728 reactor. *Proc Combust Inst* 2015;35:1887–94. <https://doi.org/10.1016/j.proci.2014.05.095>.
- 729 [42] De Falco G, Bocchicchio S, Commodo M, Minutolo P, D’Anna A. Raman spectroscopy of nascent  
730 soot oxidation: structural analysis during heating. *Front Energy Res* 2022;10:878171.
- 731 [43] Russo C, Ciajolo A, Cimino S, La Matta V, La Rocca A, Apicella B. Reactivity of soot emitted  
732 from different hydrocarbon fuels. Effect of nanostructure on oxidation kinetics. *Fuel Process*  
733 *Technol* 2022;236:107401. <https://doi.org/10.1016/j.fuproc.2022.107401>.
- 734 [44] Grimonprez S, Faccinnetto A, Batut S, Wu J, Desgroux P, Petitprez D. Cloud condensation nuclei  
735 from the activation with ozone of soot particles sampled from a kerosene diffusion flame. *Aerosol*  
736 *Sci Technol* 2018;52:814–27. <https://doi.org/10.1080/02786826.2018.1472367>.
- 737 [45] Wu J, Faccinnetto A, Grimonprez S, Batut S, Yon J, Desgroux P, et al. Influence of the dry aerosol  
738 particle size distribution and morphology on the cloud condensation nuclei activation. An  
739 experimental and theoretical investigation. *Atmos Chem Phys* 2020;20:4209–25.  
740 <https://doi.org/10.5194/acp-20-4209-2020>.
- 741 [46] Faccinnetto A, Irimiea C, Minutolo P, Commodo M, D’Anna A, Nuns N, et al. Evidence on the  
742 formation of dimers of polycyclic aromatic hydrocarbons in a laminar diffusion flame. *Commun*  
743 *Chem* 2020;3:112. <https://doi.org/10.1038/s42004-020-00357-2>.
- 744 [47] Vitiello G, De Falco G, Picca F, Commodo M, D’Errico G, Minutolo P, et al. Role of radicals in  
745 carbon clustering and soot inception: a combined EPR and Raman spectroscopic study. *Combust*  
746 *Flame* 2019;205:286–94. <https://doi.org/10.1016/j.combustflame.2019.04.028>.
- 747 [48] Elias J, Faccinnetto A, Vezin H, Mercier X. Investigation of resonance-stabilized radicals associated  
748 with soot particle inception using advanced electron paramagnetic resonance techniques. *Commun*  
749 *Chem* 2023;6:99. <https://doi.org/10.1038/s42004-023-00896-4>.
- 750 [49] Irimiea C, Faccinnetto A, Carpentier Y, Ortega I-K, Nuns N, Therssen E, et al. A comprehensive  
751 protocol for chemical analysis of flame combustion emissions by secondary ion mass spectrometry.  
752 *Rapid Commun Mass Spectrom* 2018;32:1015–25. <https://doi.org/10.1002/rcm.8133>.
- 753 [50] Mercier X, Carrivain O, Irimiea C, Faccinnetto A, Therssen E. Dimers of polycyclic aromatic  
754 hydrocarbons: the missing pieces in the soot formation process. *Phys Chem Chem Phys*  
755 2019;21:8282–94. <https://doi.org/10.1039/C9CP00394K>.

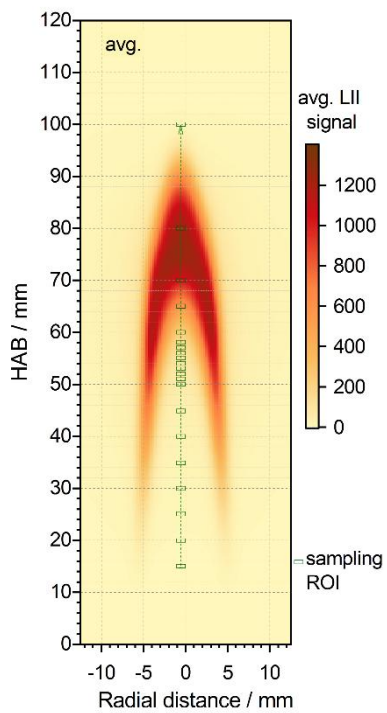
- 756 [51] Elias J, Faccineto A, Batut S, Carrivain O, Sirignano M, D'Anna A, et al. Thermocouple-based  
757 thermometry for laminar sooting flames: Implementation of a fast and simple methodology. *Int J*  
758 *Therm Sci* 2023;184:107973. <https://doi.org/10.1016/j.ijthermalsci.2022.107973>.
- 759 [52] Dobbins RA, Fletcher RA, Chang H-C. The evolution of soot precursor particles in a diffusion  
760 flame. *Combust Flame* 1998;115:285–98. [https://doi.org/10.1016/S0010-2180\(98\)00010-8](https://doi.org/10.1016/S0010-2180(98)00010-8).
- 761 [53] Casiraghi C, Piazza F, Ferrari AC, Grambole D, Robertson J. Bonding in hydrogenated diamond-  
762 like carbon by Raman spectroscopy. *Diam Relat Mater* 2005;14:1098–102.  
763 <https://doi.org/10.1016/j.diamond.2004.10.030>.
- 764 [54] Buijnsters JG, Gago R, Jiménez I, Camero M, Agulló-Rueda F, Gómez-Aleixandre C. Hydrogen  
765 quantification in hydrogenated amorphous carbon films by infrared, Raman, and x-ray absorption  
766 near edge spectroscopies. *J Appl Phys* 2009;105:093510. <https://doi.org/10.1063/1.3103326>.
- 767 [55] Parent P, Laffon C, Marhaba I, Ferry D, Regier TZ, Ortega I-K, et al. Nanoscale characterization of  
768 aircraft soot: a high-resolution transmission electron microscopy, Raman spectroscopy, X-ray  
769 photoelectron and near-edge X-ray absorption spectroscopy study. *Carbon* 2016;101:86–100.  
770 <https://doi.org/10.1016/j.carbon.2016.01.040>.
- 771 [56] Commodo M, D'Anna A, De Falco G, Larciprete R, Minutolo P. Illuminating the earliest stages of  
772 the soot formation by photoemission and Raman spectroscopy. *Combust Flame* 2017;181:188–97.  
773 <https://doi.org/10.1016/j.combustflame.2017.03.020>.
- 774 [57] Ferrari AC, Robertson J. Interpretation of Raman spectra of disordered and amorphous carbon. *Phys*  
775 *Rev B* 2000;61:14095–107. <https://doi.org/10.1103/PhysRevB.61.14095>.
- 776 [58] Le KC, Lefumeux C, Bengtsson P-E, Pino T. Direct observation of aliphatic structures in soot  
777 particles produced in low-pressure premixed ethylene flames via online Raman spectroscopy. *Proc*  
778 *Combust Inst* 2019;37:869–76. <https://doi.org/10.1016/j.proci.2018.08.003>.
- 779 [59] Sadezky A, Muckenhuber H, Grothe H, Niessner R, Pöschl U. Raman microspectroscopy of soot  
780 and related carbonaceous materials: spectral analysis and structural information. *Carbon*  
781 2005;43:1731–42. <https://doi.org/10.1016/j.carbon.2005.02.018>.
- 782 [60] Russo C, Apicella B, Lighty JS, Ciajolo A, Tregrossi A. Optical properties of organic carbon and  
783 soot produced in an inverse diffusion flame. *Carbon* 2017;124:372–9.  
784 <https://doi.org/10.1016/j.carbon.2017.08.073>.
- 785 [61] Haller T, Rentenberger C, Meyer JC, Felgitsch L, Grothe H, Hitzemberger R. Structural changes of  
786 CAST soot during a thermal–optical measurement protocol. *Atmos Meas Tech* 2019;12:3503–19.  
787 <https://doi.org/10.5194/amt-12-3503-2019>.
- 788 [62] Minutolo P, Commodo M, Santamaria A, De Falco G, D'Anna A. Characterization of flame-  
789 generated 2-D carbon nano-disks. *Carbon* 2014;68:138–48.  
790 <https://doi.org/10.1016/j.carbon.2013.10.073>.
- 791 [63] Catelani T, Pratesi G, Zoppi M. Raman characterization of ambient airborne soot and associated  
792 mineral phases. *Aerosol Sci Technol* 2014;48:13–21.  
793 <https://doi.org/10.1080/02786826.2013.847270>.
- 794 [64] Carpentier Y, Féraud G, Dartois E, Brunetto R, Charon E, Cao A-T, et al. Nanostructuring of  
795 carbonaceous dust as seen through the positions of the 6.2 and 7.7  $\mu\text{m}$  AIBs. *Astron Astrophys*  
796 2012;548:A40. <https://doi.org/10.1051/0004-6361/201118700>.
- 797 [65] Dasappa S, Camacho J. Evolution in size and structural order for incipient soot formed at flame  
798 temperatures greater than 2100 K. *Fuel* 2021;291:120196.  
799 <https://doi.org/10.1016/j.fuel.2021.120196>.
- 800 [66] Dippel B, Jander H, Heintzenberg J. NIR FT Raman spectroscopic study of flame soot. *Phys Chem*  
801 *Chem Phys* 1999;1:4707–12. <https://doi.org/10.1039/A904529E>.
- 802 [67] Cuesta A, Dhamelincourt P, Laureyns J, Martínez-Alonso A, Tascón JMD. Raman microprobe  
803 studies on carbon materials. *Carbon* 1994;32:1523–32. [https://doi.org/10.1016/0008-6223\(94\)90148-1](https://doi.org/10.1016/0008-6223(94)90148-1).
- 804

- 805 [68] Livneh T, Bar-Ziv E, Senneca O, Salatino P. Evolution of reactivity of highly porous chars from  
806 Raman microscopy. *Combust Sci Technol* 2000;153:65–82.  
807 <https://doi.org/10.1080/00102200008947251>.
- 808 [69] Tan PH, Hu CY, Dong J, Shen WC, Zhang BF. Polarization properties, high-order Raman spectra,  
809 and frequency asymmetry between Stokes and anti-Stokes scattering of Raman modes in a graphite  
810 whisker. *Phys Rev B* 2001;64:214301. <https://doi.org/10.1103/PhysRevB.64.214301>.
- 811 [70] Mafra DL, Samsonidze G, Malard LM, Elias DC, Brant JC, Plentz F, et al. Determination of LA  
812 and TO phonon dispersion relations of graphene near the Dirac point by double resonance Raman  
813 scattering. *Phys Rev B* 2007;76:233407. <https://doi.org/10.1103/PhysRevB.76.233407>.
- 814 [71] Tuinstra F, Koenig JL. Raman spectrum of graphite. *J Chem Phys* 1970;53:1126–30.  
815 <https://doi.org/10.1063/1.1674108>.
- 816 [72] Katagiri G, Ishida H, Ishitani A. Raman spectra of graphite edge planes. *Carbon* 1988;26:565–71.  
817 [https://doi.org/10.1016/0008-6223\(88\)90157-1](https://doi.org/10.1016/0008-6223(88)90157-1).
- 818 [73] Wang Y, Alsmeyer DC, McCreery RL. Raman spectroscopy of carbon materials: structural basis of  
819 observed spectra. *Chem Mater* 1990;2:557–63. <https://doi.org/10.1021/cm00011a018>.
- 820 [74] Di Donato E, Tommasini M, Fustella G, Brambilla L, Castiglioni C, Zerbi G, et al. Wavelength-  
821 dependent Raman activity of D<sub>2h</sub> symmetry polycyclic aromatic hydrocarbons in the D-band and  
822 acoustic phonon regions. *Chem Phys* 2004;301:81–93.  
823 <https://doi.org/10.1016/j.chemphys.2004.02.018>.
- 824 [75] Jawhari T, Roid A, Casado J. Raman spectroscopic characterization of some commercially available  
825 carbon black materials. *Carbon* 1995;33:1561–5. [https://doi.org/10.1016/0008-6223\(95\)00117-V](https://doi.org/10.1016/0008-6223(95)00117-V).
- 826 [76] Nemanich RJ, Solin SA. First- and second-order Raman scattering from finite-size crystals of  
827 graphite. *Phys Rev B* 1979;20:392–401. <https://doi.org/10.1103/PhysRevB.20.392>.
- 828 [77] Beyssac O, Goffé B, Petitot J-P, Froigneux E, Moreau M, Rouzaud J-N. On the characterization of  
829 disordered and heterogeneous carbonaceous materials by Raman spectroscopy. *Spectrochim Acta A*  
830 2003;59:2267–76. [https://doi.org/10.1016/S1386-1425\(03\)00070-2](https://doi.org/10.1016/S1386-1425(03)00070-2).
- 831 [78] Abdi H, Williams LJ. Principal component analysis. *Wiley Interdiscip Rev Comput Stat*  
832 2010;2:433–59. <https://doi.org/10.1002/wics.101>.
- 833 [79] Bro R, Smilde AK. Principal component analysis. *Anal Methods* 2014;6:2812–31.  
834 <https://doi.org/10.1039/C3AY41907J>.
- 835 [80] Pei L, Jiang G, Tyler BJ, Baxter LL, Linford MR. Time-of-flight secondary ion mass spectrometry  
836 of a range of coal samples: a chemometrics (PCA, cluster, and PLS) analysis. *Energ Fuels*  
837 2008;22:1059–72. <https://doi.org/10.1021/ef7003199>.
- 838 [81] Duca D, Irimiea C, Faccinetto A, Noble JA, Vojkovic M, Carpentier Y, et al. On the benefits of  
839 using multivariate analysis in mass spectrometric studies of combustion-generated aerosols. *Faraday*  
840 *Discuss* 2019;218:115–37. <https://doi.org/10.1039/C8FD00238J>.
- 841 [82] Negri F, Castiglioni C, Tommasini M, Zerbi G. A computational study of the Raman spectra of  
842 large polycyclic aromatic hydrocarbons: toward molecularly defined subunits of graphite. *J Phys*  
843 *Chem A* 2002;106:3306–17. <https://doi.org/10.1021/jp0128473>.
- 844 [83] Pimenta MA, Dresselhaus G, Dresselhaus MS, Cançado LG, Jorio A, Saito R. Studying disorder in  
845 graphite-based systems by Raman spectroscopy. *Phys Chem Chem Phys* 2007;9:1276–90.  
846 <https://doi.org/10.1039/B613962K>.
- 847 [84] Ess MN, Ferry D, Kireeva ED, Niessner R, Ouf F-X, Ivleva NP. In situ Raman microspectroscopic  
848 analysis of soot samples with different organic carbon content: structural changes during heating.  
849 *Carbon* 2016;105:572–85. <https://doi.org/10.1016/j.carbon.2016.04.056>.
- 850 [85] Baldelli A, Rogak SN. Morphology and Raman spectra of aerodynamically classified soot samples.  
851 *Atmos Meas Tech* 2019;12:4339–46. <https://doi.org/10.5194/amt-12-4339-2019>.
- 852 [86] Skrzypczak-Bonduelle A, Binet L, Delpoux O, Vezin H, Derenne S, Robert F, et al. EPR of radicals  
853 in primitive organic matter: a tool for the search of biosignatures of the most ancient traces of life.  
854 *Appl Magn Reson* 2008;33:371–97. <https://doi.org/10.1007/s00723-008-0083-y>.

- 855 [87] D'Anna A, Sirignano M, Kent J. A model of particle nucleation in premixed ethylene flames.  
856 Combust Flame 2010;157:2106–15. <https://doi.org/10.1016/j.combustflame.2010.04.019>.
- 857 [88] Beretta F, Cincotti V, D'Alessio A, Menna P. Ultraviolet and visible fluorescence in the fuel  
858 pyrolysis regions of gaseous diffusion flames. Combust Flame 1985;61:211–8.  
859 [https://doi.org/10.1016/0010-2180\(85\)90102-6](https://doi.org/10.1016/0010-2180(85)90102-6).
- 860 [89] Coe DS, Haynes BS, Steinfeldt JI. Identification of a source of argon-ion-laser excited fluorescence  
861 in sooting flames. Combust Flame 1981;43:211–4. [https://doi.org/10.1016/0010-2180\(81\)90018-3](https://doi.org/10.1016/0010-2180(81)90018-3).
- 862 [90] Smyth KC, Shaddix CR, Everest DA. Aspects of soot dynamics as revealed by measurements of  
863 broadband fluorescence and flame luminosity in flickering diffusion flames. Combust Flame  
864 1997;111:185–207. [https://doi.org/10.1016/S0010-2180\(97\)00017-5](https://doi.org/10.1016/S0010-2180(97)00017-5).
- 865 [91] Sirignano M, Collina A, Commodo M, Minutolo P, D'Anna A. Detection of aromatic hydrocarbons  
866 and incipient particles in an opposed-flow flame of ethylene by spectral and time-resolved laser  
867 induced emission spectroscopy. Combust Flame 2012;159:1663–9.  
868 <https://doi.org/10.1016/j.combustflame.2011.11.005>.
- 869 [92] Shariatmadar H, Hampp F, Lindstedt RP. Quantification of PAH concentrations in premixed  
870 turbulent flames crossing the soot inception limit. Proc Combust Inst 2021;38:1163–72.  
871 <https://doi.org/10.1016/j.proci.2020.06.359>.
- 872 [93] Martin JW, Pascazio L, Menon A, Akroyd J, Kaiser K, Schulz F, et al.  $\pi$ -diradical aromatic soot  
873 precursors in flames. J Am Chem Soc 2021;143:12212–9. <https://doi.org/10.1021/jacs.1c05030>.
- 874 [94] Sabbah H, Biennier L, Klippenstein SJ, Sims IR, Rowe BR. Exploring the role of PAHs in the  
875 formation of soot: pyrene dimerization. J Phys Chem Lett 2010;1:2962–7.  
876 <https://doi.org/10.1021/jz101033t>.
- 877 [95] Small D, Zaitsev V, Jung Y, Rosokha SV, Head-Gordon M, Kochi JK. Intermolecular  $\pi$ -to- $\pi$   
878 bonding between stacked aromatic dyads. experimental and theoretical binding energies and near-IR  
879 optical transitions for phenalenyl radical/radical versus radical/cation dimerizations. J Am Chem  
880 Soc 2004;126:13850–8. <https://doi.org/10.1021/ja046770i>.
- 881 [96] Xiang Q, Guo J, Xu J, Ding S, Li Z, Li G, et al. Stable olympicenyl radicals and their  $\pi$ -dimers. J  
882 Am Chem Soc 2020;142:11022–31. <https://doi.org/10.1021/jacs.0c02287>.
- 883 [97] Selvakumar PK, Martin JW, Lorenzo MD, Paskevicius M, Buckley CE. Role of  $\pi$ -radical  
884 localization on thermally stable cross-links between polycyclic aromatic hydrocarbons. J Phys  
885 Chem A 2023;127:6945–52. <https://doi.org/10.1021/acs.jpca.3c03769>.
- 886 [98] Faccinetto A, Focsa C, Desgroux P, Ziskind M. Progress toward the quantitative analysis of PAHs  
887 adsorbed on soot by laser desorption/laser ionization/time-of-flight mass spectrometry. Environ Sci  
888 Technol 2015;49:10510–20. <https://doi.org/10.1021/acs.est.5b02703>.
- 889

890 **8. Supporting Information**

891 **8.1 Flame sampling scheme**



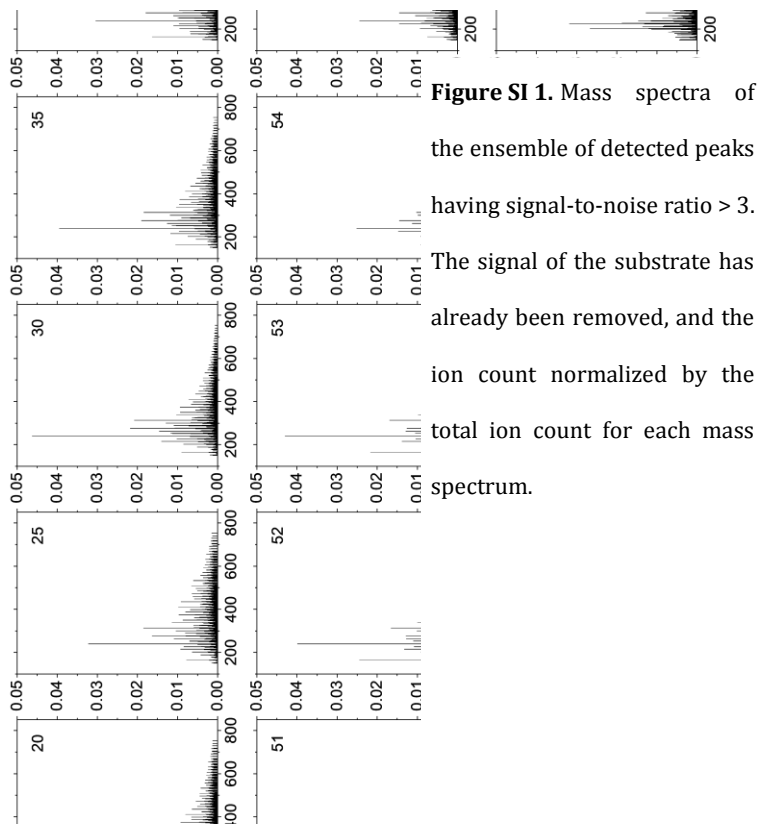
892

893 **Figure SI 1.** LII mapping of soot in the diffusion flame and sampling scheme (green hollow rectangles).

894



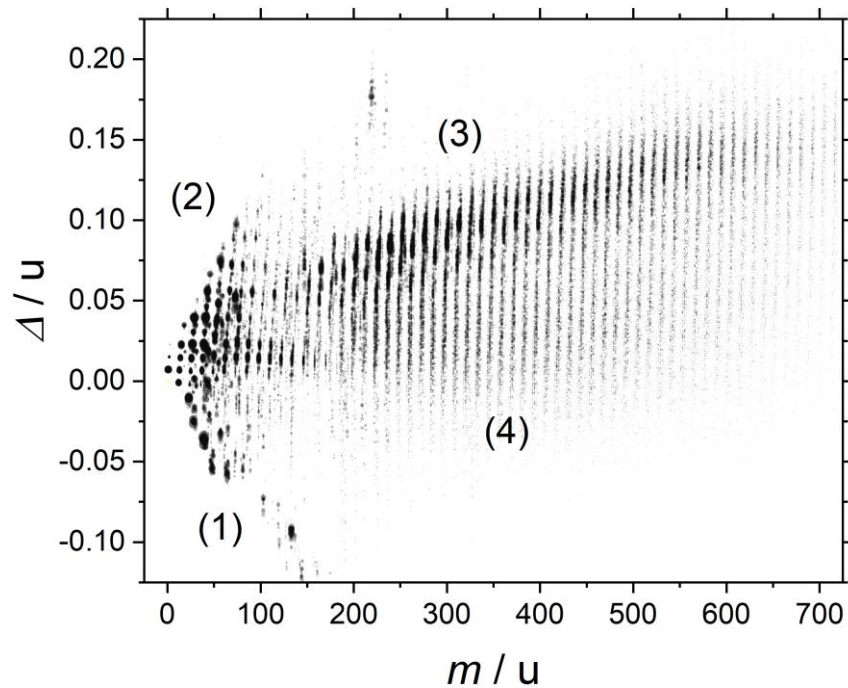
895 **8.2 ToF-SIMS mass spectra**



896

897 **8.3 ToF-SIMS mass defect analysis**

898 Figure SI 2 shows the mass defect plot obtained from the ensemble of spectra used  
899 to build the peak list in Table SI 1 and for the multivariate analysis.



900

901 **Figure SI 2.** Mass defect plot showing the ensemble of detected peaks having signal-to-noise ratio > 3. The size of the  
 902 datapoints is proportional to the logarithm of the peak intensity. The low mass defect series (1), also very prominent in  
 903 the blank, is assigned to Ti oxides from the deposition substrates. The low  $m/z$  peaks (2) bear contributions from the  
 904 blank and fragment ions. The high  $m/z$  and high mass defect peaks (3) are typical of soot and contain many identified  
 905 hydrocarbons. The high  $m/z$  and low mass defect peaks (4), also typical of soot, are consistent with oxygen-containing  
 906 hydrocarbons or low-hydrogen carbon cluster ions, however, certain assignments are not possible with the limited  
 907 available resolving power ( $m/\Delta m \approx 104$  at 200  $m/z$ ) [46].

908

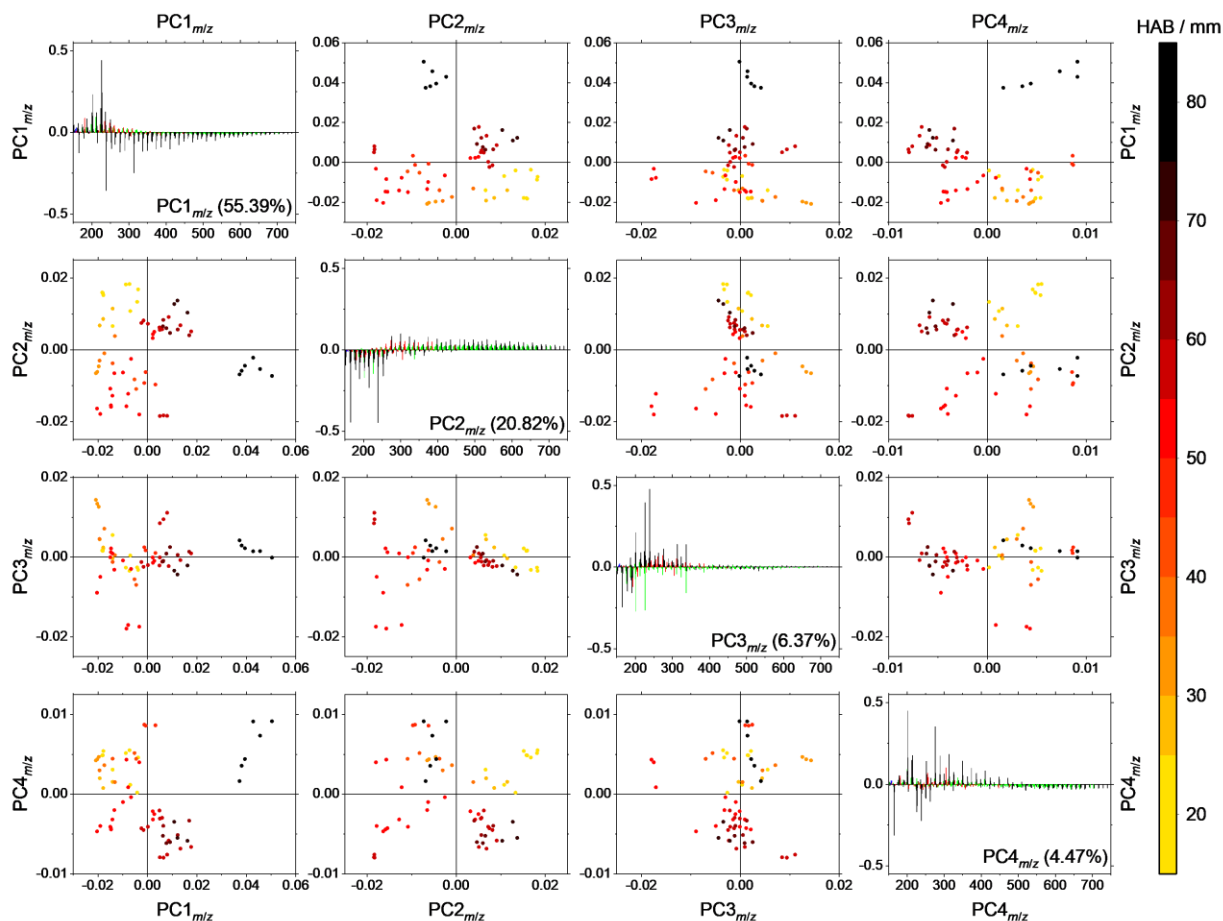
909 **Table SI 1. Peak list used in the data reduction.** The 95% confidence level on the *m/z* is shown between brackets.

<i>m/z</i>	Formula	<i>m/z</i>	Formula	<i>m/z</i>	Formula	<i>m/z</i>	Formula	<i>m/z</i>	Formula
150.02(2)	?	224.06(2)	C <sub>18</sub> H <sub>8</sub> <sup>+</sup>	303.12(3)	[ <sup>13</sup> C] <sub>24</sub> H <sub>14</sub> <sup>+</sup>	394.02(4)	?	511.14(5)	C <sub>42</sub> H <sub>19</sub> <sup>+</sup>
150.04(2)	C <sub>12</sub> H <sub>6</sub> <sup>+</sup>	225.03(2)	?	304.12(3)	C <sub>24</sub> H <sub>16</sub>	395.03(4)	?	512.15(5)	[ <sup>13</sup> C] <sub>41</sub> H <sub>19</sub> <sup>+</sup>
151.03(2)	?	225.06(2)	[ <sup>13</sup> C] <sub>18</sub> H <sub>8</sub> <sup>+</sup>	305.10(3)	C <sub>23</sub> H <sub>13</sub> O <sup>+</sup>	396.04(4)	?	513.15(5)	?
151.05(2)	[ <sup>13</sup> C] <sub>12</sub> H <sub>6</sub> <sup>+</sup>	226.05(2)	?	306.10(3)	[ <sup>13</sup> C] <sub>23</sub> H <sub>13</sub> O <sup>+</sup>	397.06(4)	?	516.03(5)	?
152.03(2)	?	226.08(2)	C <sub>18</sub> H <sub>10</sub> <sup>+</sup>	307.01(3)	?	398.10(4)	C <sub>32</sub> H <sub>14</sub> <sup>+</sup>	518.05(5)	?
152.06(2)	C <sub>12</sub> H <sub>8</sub> <sup>+</sup>	226.82(2)	?	309.02(3)	?	399.11(4)	[ <sup>13</sup> C] <sub>32</sub> H <sub>14</sub> <sup>+</sup>	519.06(5)	?
153.04(2)	?	227.08(2)	[ <sup>13</sup> C] <sub>18</sub> H <sub>10</sub> <sup>+</sup>	309.05(3)	C <sub>21</sub> H <sub>9</sub> O <sub>3</sub> <sup>+</sup>	400.12(4)	C <sub>32</sub> H <sub>16</sub>	520.12(5)	C <sub>42</sub> H <sub>16</sub> <sup>+</sup>
153.07(2)	[ <sup>13</sup> C] <sub>12</sub> H <sub>8</sub> <sup>+</sup>	228.09(2)	C <sub>18</sub> H <sub>12</sub> <sup>+</sup>	310.04(3)	[ <sup>13</sup> C] <sub>21</sub> H <sub>9</sub> O <sub>3</sub> <sup>+</sup>	401.13(4)	[ <sup>13</sup> C] <sub>32</sub> H <sub>16</sub> <sup>+</sup>	521.13(5)	[ <sup>13</sup> C] <sub>42</sub> H <sub>16</sub> <sup>+</sup>
154.04(2)	?	229.07(2)	C <sub>17</sub> H <sub>9</sub> O <sup>+</sup>	311.03(3)	?	402.13(4)	?	522.14(5)	C <sub>42</sub> H <sub>18</sub> <sup>+</sup>
154.07(2)	C <sub>11</sub> H <sub>8</sub> N <sup>+</sup>	229.10(2)	[ <sup>13</sup> C] <sub>18</sub> H <sub>12</sub> <sup>+</sup>	311.07(3)	C <sub>21</sub> H <sub>11</sub> O <sub>3</sub> <sup>+</sup>	403.12(4)	?	523.15(5)	[ <sup>13</sup> C] <sub>42</sub> H <sub>18</sub> <sup>+</sup>
155.05(2)	C <sub>11</sub> H <sub>7</sub> O <sup>+</sup>	230.07(2)	[ <sup>13</sup> C] <sub>17</sub> H <sub>9</sub> O <sup>+</sup>	312.08(3)	[ <sup>13</sup> C] <sub>21</sub> H <sub>11</sub> O <sub>3</sub> <sup>+</sup>	404.12(4)	C <sub>31</sub> H <sub>16</sub> O <sup>+</sup>	524.15(5)	C <sub>42</sub> H <sub>20</sub> <sup>+</sup>
155.09(2)	C <sub>12</sub> H <sub>11</sub> <sup>+</sup>	230.11(2)	?	313.10(3)	C <sub>25</sub> H <sub>13</sub> <sup>+</sup>	405.01(4)	?	525.15(5)	[ <sup>13</sup> C] <sub>42</sub> H <sub>20</sub> <sup>+</sup>
156.09(2)	C <sub>11</sub> H <sub>10</sub> N <sup>+</sup>	231.08(2)	C <sub>17</sub> H <sub>11</sub> O <sup>+</sup>	314.10(3)	[ <sup>13</sup> C] <sub>25</sub> H <sub>13</sub> <sup>+</sup>	405.12(4)	[ <sup>13</sup> C] <sub>31</sub> H <sub>16</sub> O <sup>+</sup>	529.04(5)	?
157.07(2)	C <sub>11</sub> H <sub>9</sub> O <sup>+</sup>	232.09(2)	[ <sup>13</sup> C] <sub>17</sub> H <sub>11</sub> O <sup>+</sup>	315.11(3)	C <sub>25</sub> H <sub>15</sub> <sup>+</sup>	407.03(4)	?	531.07(5)	?
158.10(2)	C <sub>11</sub> H <sub>12</sub> N <sup>+</sup>	233.00(2)	?	316.10(3)	C <sub>24</sub> H <sub>15</sub> O <sup>+</sup>	408.03(4)	?	533.13(5)	C <sub>43</sub> H <sub>17</sub> <sup>+</sup>
159.08(2)	C <sub>11</sub> H <sub>11</sub> O <sup>+</sup>	233.06(2)	C <sub>16</sub> H <sub>9</sub> O <sub>2</sub> <sup>+</sup>	317.10(3)	[ <sup>13</sup> C] <sub>24</sub> H <sub>12</sub> O <sup>+</sup>	409.05(4)	?	534.14(5)	[ <sup>13</sup> C] <sub>43</sub> H <sub>17</sub> <sup>+</sup>
161.00(2)	?	234.01(2)	?	318.00(3)	?	409.08(4)	?	535.15(5)	C <sub>43</sub> H <sub>19</sub> <sup>+</sup>
161.04(2)	C <sub>13</sub> H <sub>5</sub> <sup>+</sup>	235.01(2)	?	318.11(3)	?	410.08(4)	?	536.15(5)	[ <sup>13</sup> C] <sub>43</sub> H <sub>19</sub> <sup>+</sup>
162.02(2)	?	235.04(2)	C <sub>15</sub> H <sub>7</sub> O <sub>3</sub> <sup>+</sup>	319.11(3)	?	411.12(4)	C <sub>33</sub> H <sub>15</sub> <sup>+</sup>	537.15(5)	?
162.04(2)	[ <sup>13</sup> C] <sub>13</sub> H <sub>5</sub> <sup>+</sup>	236.02(2)	?	320.01(3)	?	412.12(4)	[ <sup>13</sup> C] <sub>33</sub> H <sub>15</sub> <sup>+</sup>	540.03(5)	?
163.03(2)	?	236.04(2)	[ <sup>13</sup> C] <sub>15</sub> H <sub>7</sub> O <sub>3</sub> <sup>+</sup>	321.02(3)	?	413.13(4)	C <sub>33</sub> H <sub>17</sub> <sup>+</sup>	542.05(5)	?
163.05(2)	C <sub>13</sub> H <sub>7</sub> <sup>+</sup>	237.03(2)	?	322.02(3)	?	414.13(4)	[ <sup>13</sup> C] <sub>33</sub> H <sub>17</sub> <sup>+</sup>	544.10(5)	?
164.03(2)	?	237.07(2)	C <sub>19</sub> H <sub>9</sub> <sup>+</sup>	322.05(3)	?	415.13(4)	?	545.11(5)	?
164.06(2)	[ <sup>13</sup> C] <sub>13</sub> H <sub>7</sub> <sup>+</sup>	238.04(2)	?	323.05(3)	?	416.00(4)	?	546.14(5)	C <sub>44</sub> H <sub>18</sub> <sup>+</sup>
165.07(2)	C <sub>13</sub> H <sub>9</sub> <sup>+</sup>	238.07(2)	[ <sup>13</sup> C] <sub>19</sub> H <sub>9</sub> <sup>+</sup>	324.04(3)	?	416.12(4)	C <sub>32</sub> H <sub>16</sub> O <sup>+</sup>	547.15(5)	[ <sup>13</sup> C] <sub>44</sub> H <sub>18</sub> <sup>+</sup>
166.08(2)	[ <sup>13</sup> C] <sub>13</sub> H <sub>9</sub> <sup>+</sup>	239.09(2)	C <sub>19</sub> H <sub>11</sub> <sup>+</sup>	324.08(3)	C <sub>28</sub> H <sub>12</sub> <sup>+</sup>	417.13(4)	[ <sup>13</sup> C] <sub>32</sub> H <sub>16</sub> O <sup>+</sup>	548.15(5)	C <sub>44</sub> H <sub>20</sub> <sup>+</sup>
167.09(2)	C <sub>13</sub> H <sub>11</sub> <sup>+</sup>	240.09(2)	[ <sup>13</sup> C] <sub>19</sub> H <sub>11</sub> <sup>+</sup>	325.10(3)	[ <sup>13</sup> C] <sub>28</sub> H <sub>12</sub> <sup>+</sup>	418.02(4)	?	549.16(5)	[ <sup>13</sup> C] <sub>44</sub> H <sub>20</sub> <sup>+</sup>
168.06(2)	C <sub>12</sub> H <sub>8</sub> O <sup>+</sup>	241.10(2)	C <sub>19</sub> H <sub>13</sub> <sup>+</sup>	326.11(3)	C <sub>26</sub> H <sub>14</sub> <sup>+</sup>	420.04(4)	?	550.15(6)	?
169.07(2)	C <sub>12</sub> H <sub>9</sub> O <sup>+</sup>	242.08(2)	C <sub>18</sub> H <sub>10</sub> O <sup>+</sup>	327.12(3)	[ <sup>13</sup> C] <sub>26</sub> H <sub>14</sub> <sup>+</sup>	421.04(4)	?	553.04(6)	?
174.01(2)	?	243.08(2)	[ <sup>13</sup> C] <sub>18</sub> H <sub>10</sub> O <sup>+</sup>	328.12(3)	C <sub>28</sub> H <sub>16</sub>	422.10(4)	C <sub>34</sub> H <sub>14</sub> <sup>+</sup>	555.06(6)	?
174.05(2)	C <sub>14</sub> H <sub>6</sub> <sup>+</sup>	244.09(2)	C <sub>18</sub> H <sub>12</sub> O <sup>+</sup>	329.10(3)	C <sub>28</sub> H <sub>13</sub> O <sup>+</sup>	423.11(4)	[ <sup>13</sup> C] <sub>34</sub> H <sub>14</sub> <sup>+</sup>	557.13(6)	C <sub>45</sub> H <sub>17</sub> <sup>+</sup>
175.02(2)	?	245.10(2)	[ <sup>13</sup> C] <sub>18</sub> H <sub>12</sub> O <sup>+</sup>	330.10(3)	[ <sup>13</sup> C] <sub>25</sub> H <sub>13</sub> O <sup>+</sup>	424.12(4)	C <sub>34</sub> H <sub>16</sub> <sup>+</sup>	558.14(6)	[ <sup>13</sup> C] <sub>45</sub> H <sub>17</sub> <sup>+</sup>
175.05(2)	[ <sup>13</sup> C] <sub>14</sub> H <sub>6</sub> <sup>+</sup>	246.00(2)	?	331.00(3)	?	425.13(4)	[ <sup>13</sup> C] <sub>34</sub> H <sub>16</sub> <sup>+</sup>	559.15(6)	C <sub>45</sub> H <sub>19</sub> <sup>+</sup>
176.03(2)	?	246.03(2)	?	333.02(3)	?	426.14(4)	C <sub>34</sub> H <sub>18</sub>	560.15(6)	[ <sup>13</sup> C] <sub>45</sub> H <sub>19</sub> <sup>+</sup>
176.06(2)	C <sub>14</sub> H <sub>8</sub> <sup>+</sup>	247.02(2)	?	334.03(3)	?	427.14(4)	[ <sup>13</sup> C] <sub>34</sub> H <sub>18</sub> <sup>+</sup>	561.15(6)	?
177.04(2)	?	248.02(2)	?	335.03(3)	?	428.14(4)	?	562.16(6)	?
177.07(2)	[ <sup>13</sup> C] <sub>14</sub> H <sub>8</sub> <sup>+</sup>	248.05(2)	C <sub>16</sub> H <sub>8</sub> O <sub>3</sub> <sup>+</sup>	335.07(3)	C <sub>23</sub> H <sub>11</sub> O <sub>3</sub> <sup>+</sup>	428.71(4)	?	566.04(6)	?
178.05(2)	?	249.03(2)	?	336.07(3)	[ <sup>13</sup> C] <sub>23</sub> H <sub>11</sub> O <sub>3</sub> <sup>+</sup>	429.00(4)	?	568.09(6)	?
178.08(2)	C <sub>14</sub> H <sub>10</sub> <sup>+</sup>	249.05(2)	[ <sup>13</sup> C] <sub>16</sub> H <sub>8</sub> O <sub>3</sub> <sup>+</sup>	337.04(3)	?	429.13(4)	C <sub>33</sub> H <sub>17</sub> O <sup>+</sup>	569.09(6)	?
179.05(2)	?	250.04(3)	?	337.10(3)	C <sub>27</sub> H <sub>13</sub> <sup>+</sup>	431.02(4)	?	570.14(6)	C <sub>46</sub> H <sub>18</sub> <sup>+</sup>
179.09(2)	C <sub>14</sub> H <sub>11</sub> <sup>+</sup>	250.07(3)	C <sub>20</sub> H <sub>10</sub> <sup>+</sup>	338.10(3)	[ <sup>13</sup> C] <sub>27</sub> H <sub>13</sub> <sup>+</sup>	433.05(4)	?	571.15(6)	[ <sup>13</sup> C] <sub>46</sub> H <sub>18</sub> <sup>+</sup>
180.09(2)	[ <sup>13</sup> C] <sub>14</sub> H <sub>11</sub> <sup>+</sup>	251.08(3)	[ <sup>13</sup> C] <sub>20</sub> H <sub>10</sub> <sup>+</sup>	339.12(3)	C <sub>27</sub> H <sub>15</sub> <sup>+</sup>	434.07(4)	?	572.15(6)	C <sub>46</sub> H <sub>20</sub> <sup>+</sup>
181.07(2)	C <sub>13</sub> H <sub>9</sub> O <sup>+</sup>	252.09(3)	C <sub>20</sub> H <sub>12</sub>	340.12(3)	[ <sup>13</sup> C] <sub>27</sub> H <sub>15</sub> <sup>+</sup>	435.12(4)	C <sub>35</sub> H <sub>15</sub> <sup>+</sup>	573.16(6)	[ <sup>13</sup> C] <sub>46</sub> H <sub>20</sub> <sup>+</sup>
182.07(2)	[ <sup>13</sup> C] <sub>13</sub> H <sub>9</sub> O <sup>+</sup>	253.10(3)	[ <sup>13</sup> C] <sub>20</sub> H <sub>12</sub> <sup>+</sup>	341.13(3)	C <sub>27</sub> H <sub>17</sub> <sup>+</sup>	436.12(4)	[ <sup>13</sup> C] <sub>35</sub> H <sub>15</sub> <sup>+</sup>	574.16(6)	?
183.05(2)	C <sub>12</sub> H <sub>7</sub> O <sub>2</sub> <sup>+</sup>	254.11(3)	C <sub>20</sub> H <sub>14</sub> <sup>+</sup>	342.13(3)	?	437.13(4)	C <sub>35</sub> H <sub>17</sub> <sup>+</sup>	577.03(6)	?
185.00(2)	?	255.08(3)	C <sub>19</sub> H <sub>11</sub> O <sup>+</sup>	343.11(3)	C <sub>26</sub> H <sub>15</sub> O <sup>+</sup>	438.13(4)	[ <sup>13</sup> C] <sub>35</sub> H <sub>17</sub> <sup>+</sup>	579.06(6)	?
185.03(2)	?	256.09(3)	[ <sup>13</sup> C] <sub>19</sub> H <sub>11</sub> O <sup>+</sup>	344.01(3)	?	439.14(4)	?	581.13(6)	C <sub>47</sub> H <sub>17</sub> <sup>+</sup>
186.01(2)	?	256.99(3)	?	345.02(3)	?	440.14(4)	?	582.14(6)	[ <sup>13</sup> C] <sub>47</sub> H <sub>17</sub> <sup>+</sup>
187.02(2)	?	257.06(3)	C <sub>18</sub> H <sub>9</sub> O <sub>2</sub> <sup>+</sup>	346.03(3)	?	442.01(4)	?	583.15(6)	C <sub>47</sub> H <sub>19</sub> <sup>+</sup>
187.05(2)	C <sub>15</sub> H <sub>7</sub> <sup>+</sup>	258.01(3)	?	347.04(3)	?	444.03(4)	?	584.15(6)	[ <sup>13</sup> C] <sub>47</sub> H <sub>19</sub> <sup>+</sup>
188.03(2)	?	258.07(3)	[ <sup>13</sup> C] <sub>18</sub> H <sub>9</sub> O <sub>2</sub> <sup>+</sup>	348.04(3)	?	445.04(4)	?	585.16(6)	?
188.06(2)	[ <sup>13</sup> C] <sub>15</sub> H <sub>7</sub> <sup>+</sup>	259.01(3)	?	348.08(3)	C <sub>24</sub> H <sub>12</sub> O <sub>3</sub> <sup>+</sup>	446.09(4)	C <sub>32</sub> H <sub>14</sub> O <sub>3</sub> <sup>+</sup>	586.16(6)	?
189.04(2)	?	259.04(3)	C <sub>17</sub> H <sub>7</sub> O <sub>3</sub> <sup>+</sup>	349.08(3)	[ <sup>13</sup> C] <sub>24</sub> H <sub>12</sub> O <sub>3</sub> <sup>+</sup>	447.10(4)	[ <sup>13</sup> C] <sub>32</sub> H <sub>14</sub> O <sub>3</sub> <sup>+</sup>	590.04(6)	?
189.07(2)	C <sub>15</sub> H <sub>9</sub> <sup>+</sup>	260.03(3)	?	350.10(4)	C <sub>28</sub> H <sub>14</sub> <sup>+</sup>	448.12(4)	C <sub>36</sub> H <sub>16</sub> <sup>+</sup>	592.07(6)	?
190.05(2)	?	261.03(3)	?	351.11(4)	[ <sup>13</sup> C] <sub>28</sub> H <sub>14</sub> <sup>+</sup>	449.13(4)	[ <sup>13</sup> C] <sub>36</sub> H <sub>16</sub> <sup>+</sup>	594.14(6)	C <sub>48</sub> H <sub>18</sub> <sup>+</sup>
190.07(2)	[ <sup>13</sup> C] <sub>15</sub> H <sub>9</sub> <sup>+</sup>	261.06(3)	C <sub>17</sub> H <sub>9</sub> O <sub>3</sub> <sup>+</sup>	352.12(4)	C <sub>28</sub> H <sub>16</sub>	450.13(5)	C <sub>36</sub> H <sub>18</sub>	595.15(6)	[ <sup>13</sup> C] <sub>48</sub> H <sub>18</sub> <sup>+</sup>
191.09(2)	C <sub>15</sub> H <sub>11</sub> <sup>+</sup>	262.03(3)	?	353.13(4)	[ <sup>13</sup> C] <sub>28</sub> H <sub>16</sub> <sup>+</sup>	451.14(5)	[ <sup>13</sup> C] <sub>36</sub> H <sub>18</sub> <sup>+</sup>	596.16(6)	C <sub>48</sub> H <sub>20</sub> <sup>+</sup>
192.09(2)	[ <sup>13</sup> C] <sub>15</sub> H <sub>11</sub> <sup>+</sup>	262.06(3)	[ <sup>13</sup> C] <sub>17</sub> H <sub>9</sub> O <sub>3</sub> <sup>+</sup>	354.14(4)	C <sub>28</sub> H <sub>18</sub> <sup>+</sup>	452.14(5)	?	597.16(6)	[ <sup>13</sup> C] <sub>48</sub> H <sub>20</sub> <sup>+</sup>
193.07(2)	C <sub>14</sub> H <sub>7</sub> O <sup>+</sup>	263.08(3)	C <sub>21</sub> H <sub>11</sub> <sup>+</sup>	355.00(4)	?	453.00(5)	?	598.16(6)	?
193.10(2)	C <sub>15</sub> H <sub>13</sub> <sup>+</sup>	264.09(3)	[ <sup>13</sup> C] <sub>21</sub> H <sub>11</sub> <sup>+</sup>	355.12(4)	C <sub>27</sub> H <sub>15</sub> O <sup>+</sup>	453.13(5)	C <sub>35</sub> H <sub>17</sub> O <sup>+</sup>	603.05(6)	?
194.01(2)	?	265.10(3)	C <sub>21</sub> H <sub>13</sub>	357.02(4)	?	455.02(5)	?	605.10(6)	?
194.08(2)	?	266.11(3)	[ <sup>13</sup> C] <sub>21</sub> H <sub>13</sub> <sup>+</sup>	357.09(4)	C <sub>28</sub> H <sub>13</sub> O <sub>2</sub> <sup>+</sup>	457.05(5)	?	607.15(6)	C <sub>49</sub> H <sub>19</sub> <sup>+</sup>
194.10(2)	C <sub>14</sub> H <sub>12</sub> N <sup>+</sup>	267.09(3)	?	358.02(4)	?	458.05(5)	?	608.16(6)	[ <sup>13</sup> C] <sub>49</sub> H <sub>19</sub> <sup>+</sup>
195.09(2)	C <sub>14</sub> H <sub>11</sub> O <sup>+</sup>	267.12(3)	C <sub>21</sub> H <sub>15</sub> <sup>+</sup>	358.10(4)	[ <sup>13</sup> C] <sub>26</sub> H <sub>13</sub> O <sub>2</sub> <sup>+</sup>	459.12(5)	C <sub>37</sub> H <sub>15</sub> <sup>+</sup>	609.16(6)	C <sub>49</sub> H <sub>21</sub> <sup>+</sup>
197.06(2)	C <sub>13</sub> H <sub>9</sub> O <sub>2</sub> <sup>+</sup>	268.09(3)	C <sub>20</sub> H <sub>12</sub> O <sup>+</sup>	359.04(4)	?	460.12(5)	[ <sup>13</sup> C] <sub>37</sub> H <sub>15</sub> <sup>+</sup>	616.06(6)	?
198.01(2)	?	269.10(3)	C <sub>20</sub> H <sub>13</sub> O <sup>+</sup>	360.05(4)	?	461.13(5)	C <sub>37</sub> H <sub>17</sub> <sup>+</sup>	618.13(6)	C <sub>50</sub> H <sub>18</sub> <sup>+</sup>
198.04(2)	?	270.01(3)	?	361.09(4)	C <sub>28</sub> H <sub>13</sub> <sup>+</sup>	462.14(5)	[ <sup>13</sup> C] <sub>37</sub> H <sub>17</sub> <sup>+</sup>	619.15(6)	[ <sup>13</sup> C] <sub>50</sub> H <sub>18</sub> <sup>+</sup>
199.02(2)	?	271.02(3)	?	362.10(4)	[ <sup>13</sup> C] <sub>28</sub> H <sub>13</sub> <sup>+</sup>	463.14(5)	?	620.15(6)	C <sub>50</sub> H <sub>20</sub> <sup>+</sup>
199.04(2)	?	272.02(3)	?	363.11(4)	C <sub>29</sub> H <sub>15</sub>	464.14(5)	?	621.16(6)	[ <sup>13</sup> C] <sub>50</sub> H <sub>20</sub> <sup>+</sup>
200.03(2)	?	272.05(3)	C <sub>18</sub> H <sub>8</sub> O <sub>3</sub> <sup>+</sup>	364.12(4)	[ <sup>13</sup> C] <sub>29</sub> H <sub>15</sub> <sup>+</sup>	466.01(5)	?	622.16(6)	?
200.06(2)	C <sub>16</sub> H <sub>8</sub> <sup>+</sup>	273.05(3)	[ <sup>13</sup> C] <sub>18</sub> H <sub>8</sub> O <sub>3</sub> <sup>+</sup>	365.13(4)	C <sub>29</sub> H <sub>17</sub> <sup>+</sup>	468.03(5)	?	627.05(6)	?
201.04(2)	?	274.03(3)	?	366.14(4)	[ <sup>13</sup> C] <sub>29</sub> H <sub>17</sub> <sup>+</sup>	470.06(5)	?	629.09(6)	?
201.07(2)	[ <sup>13</sup> C] <sub>16</sub> H <sub>8</sub> <sup>+</sup>	274.07(3)	C <sub>18</sub> H <sub>10</sub> O <sub>3</sub> <sup>+</sup>	367.13(4)	?	471.08(5)	?	631.15(6)	C <sub>51</sub> H <sub>19</sub> <sup>+</sup>
202.05(2)	?	275.07(3)	[ <sup>13</sup> C] <sub>18</sub> H <sub>10</sub> O <sub>3</sub> <sup>+</sup>	368.01(4)	?	472.12(5)	C <sub>38</sub> H <sub>16</sub> <sup>+</sup>	632.15(6)	[ <sup>13</sup> C] <sub>51</sub> H <sub>19</sub> <sup>+</sup>
202.08(2)	C <sub>16</sub> H <sub>10</sub> <sup>+</sup>	276.09(3)	C <sub>22</sub> H <sub>12</sub>	370.02(4)	?				

206.10(2)	?	284.03(3)	?	374.10(4)	C <sub>30</sub> H <sub>14</sub> <sup>+</sup>	484.11(5)	[ <sup>13</sup> C] <sub>30</sub> H <sub>15</sub> <sup>+</sup>	653.07(7)	?
207.08(2)	C <sub>15</sub> H <sub>11</sub> O <sup>+</sup>	285.02(3)	?	375.11(4)	[ <sup>13</sup> C] <sub>30</sub> H <sub>14</sub> <sup>+</sup>	485.13(5)	C <sub>30</sub> H <sub>17</sub> <sup>+</sup>	655.15(7)	C <sub>53</sub> H <sub>19</sub> <sup>+</sup>
210.01(2)	?	285.06(3)	C <sub>19</sub> H <sub>9</sub> O <sub>3</sub> <sup>+</sup>	376.12(4)	C <sub>30</sub> H <sub>16</sub> <sup>+</sup>	486.14(5)	[ <sup>13</sup> C] <sub>30</sub> H <sub>17</sub> <sup>+</sup>	656.16(7)	[ <sup>13</sup> C] <sub>53</sub> H <sub>19</sub> <sup>+</sup>
211.02(2)	?	286.06(3)	[ <sup>13</sup> C] <sub>19</sub> H <sub>9</sub> O <sub>3</sub> <sup>+</sup>	377.12(4)	[ <sup>13</sup> C] <sub>30</sub> H <sub>16</sub> <sup>+</sup>	487.14(5)	C <sub>30</sub> H <sub>19</sub> <sup>+</sup>	657.16(7)	C <sub>53</sub> H <sub>21</sub> <sup>+</sup>
211.05(2)	?	287.08(3)	C <sub>23</sub> H <sub>11</sub> <sup>+</sup>	378.13(4)	?	488.14(5)	[ <sup>13</sup> C] <sub>30</sub> H <sub>19</sub> <sup>+</sup>	664.06(7)	?
212.02(2)	?	288.08(3)	[ <sup>13</sup> C] <sub>23</sub> H <sub>11</sub> <sup>+</sup>	379.11(4)	C <sub>23</sub> H <sub>12</sub> O <sup>+</sup>	489.15(5)	?	666.10(7)	?
212.05(2)	?	289.10(3)	C <sub>23</sub> H <sub>13</sub> <sup>+</sup>	380.12(4)	[ <sup>13</sup> C] <sub>23</sub> H <sub>12</sub> O <sup>+</sup>	490.01(5)	?	668.15(7)	C <sub>54</sub> H <sub>20</sub> <sup>+</sup>
213.03(2)	?	290.11(3)	[ <sup>13</sup> C] <sub>23</sub> H <sub>13</sub> <sup>+</sup>	381.02(4)	?	492.03(5)	?	669.16(7)	[ <sup>13</sup> C] <sub>54</sub> H <sub>20</sub> <sup>+</sup>
213.07(2)	C <sub>17</sub> H <sub>9</sub> <sup>+</sup>	291.12(3)	C <sub>23</sub> H <sub>15</sub> <sup>+</sup>	381.13(4)	C <sub>29</sub> H <sub>17</sub> O <sup>+</sup>	494.06(5)	?	670.17(7)	C <sub>54</sub> H <sub>22</sub> <sup>+</sup>
214.07(2)	[ <sup>13</sup> C] <sub>17</sub> H <sub>9</sub> <sup>+</sup>	292.09(3)	C <sub>22</sub> H <sub>12</sub> O <sup>+</sup>	383.03(4)	?	495.07(5)	?	679.14(7)	C <sub>55</sub> H <sub>19</sub> <sup>+</sup>
215.09(2)	C <sub>17</sub> H <sub>11</sub> <sup>+</sup>	293.10(3)	[ <sup>13</sup> C] <sub>22</sub> H <sub>12</sub> O <sup>+</sup>	384.04(4)	?	496.12(5)	C <sub>40</sub> H <sub>16</sub> <sup>+</sup>	680.15(7)	[ <sup>13</sup> C] <sub>55</sub> H <sub>19</sub> <sup>+</sup>
216.09(2)	[ <sup>13</sup> C] <sub>17</sub> H <sub>11</sub> <sup>+</sup>	294.00(3)	?	385.04(4)	?	497.13(5)	[ <sup>13</sup> C] <sub>40</sub> H <sub>16</sub> <sup>+</sup>	681.16(7)	C <sub>55</sub> H <sub>21</sub> <sup>+</sup>
217.07(2)	?	295.01(3)	?	385.08(4)	C <sub>27</sub> H <sub>13</sub> O <sub>3</sub> <sup>+</sup>	498.14(5)	C <sub>40</sub> H <sub>18</sub> <sup>+</sup>	692.15(7)	C <sub>56</sub> H <sub>20</sub> <sup>+</sup>
217.10(2)	C <sub>17</sub> H <sub>13</sub> <sup>+</sup>	296.01(3)	?	386.09(4)	[ <sup>13</sup> C] <sub>27</sub> H <sub>13</sub> O <sub>3</sub> <sup>+</sup>	499.15(5)	[ <sup>13</sup> C] <sub>40</sub> H <sub>18</sub> <sup>+</sup>	693.16(7)	[ <sup>13</sup> C] <sub>56</sub> H <sub>20</sub> <sup>+</sup>
218.08(2)	C <sub>16</sub> H <sub>10</sub> O <sup>+</sup>	296.04(3)	?	387.11(4)	C <sub>31</sub> H <sub>15</sub> <sup>+</sup>	500.14(5)	?	694.16(7)	?
219.08(2)	[ <sup>13</sup> C] <sub>16</sub> H <sub>10</sub> O <sup>+</sup>	297.04(3)	?	388.12(4)	[ <sup>13</sup> C] <sub>31</sub> H <sub>15</sub> <sup>+</sup>	501.15(5)	?	703.13(7)	?
220.09(2)	?	298.03(3)	?	389.12(4)	?	503.03(5)	?	705.16(7)	C <sub>57</sub> H <sub>21</sub> <sup>+</sup>
220.83(2)	?	298.06(3)	C <sub>20</sub> H <sub>10</sub> O <sub>3</sub> <sup>+</sup>	390.13(4)	?	505.04(5)	?	716.15(7)	C <sub>58</sub> H <sub>20</sub> <sup>+</sup>
222.01(2)	?	299.07(3)	[ <sup>13</sup> C] <sub>20</sub> H <sub>10</sub> O <sub>3</sub> <sup>+</sup>	391.13(4)	?	507.08(5)	?	718.16(7)	C <sub>59</sub> H <sub>22</sub> <sup>+</sup>
222.03(2)	C <sub>14</sub> H <sub>6</sub> O <sub>3</sub> <sup>+</sup>	300.09(3)	C <sub>24</sub> H <sub>12</sub> <sup>+</sup>	392.00(4)	?	508.10(5)	?	729.16(7)	C <sub>59</sub> H <sub>21</sub> <sup>+</sup>
223.02(2)	?	301.10(3)	[ <sup>13</sup> C] <sub>24</sub> H <sub>12</sub> <sup>+</sup>	392.12(4)	C <sub>30</sub> H <sub>16</sub> O <sup>+</sup>	509.14(5)	C <sub>41</sub> H <sub>17</sub> <sup>+</sup>	740.15(7)	C <sub>60</sub> H <sub>20</sub> <sup>+</sup>
224.03(2)	?	302.11(3)	C <sub>24</sub> H <sub>14</sub> <sup>+</sup>	393.13(4)	[ <sup>13</sup> C] <sub>30</sub> H <sub>16</sub> O <sup>+</sup>	510.14(5)	[ <sup>13</sup> C] <sub>41</sub> H <sub>17</sub> <sup>+</sup>	753.16(8)	C <sub>61</sub> H <sub>21</sub> <sup>+</sup>

910

## 911 8.4 PCA on the ToF-SIMS mass spectra



912

913 **Figure SI 3. Results of the PCA (covariance matrix) performed on the mass spectra of the impactation ROIs.** The  
914 figure shows the score plots of the first four principal components and the corresponding loading plots in the main  
915 diagonal. The scores are color-mapped on the sampling HAB (scale on the side of the figure). The loadings are  
916 color-mapped on the assigned formula:  $C_mH_n^+$  (black),  $C_mH_nO_p^+$  (red) and unassigned (green).

917

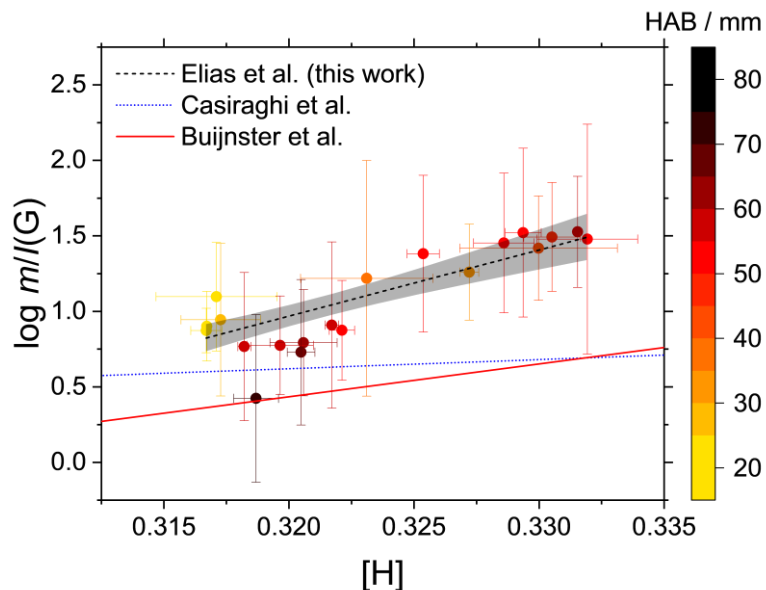
## 918 **8.5 Calculating [H] from the Raman spectra**

919 In Raman spectroscopy, [H] of organic films has been shown to be proportional to  $\log m/I(G)$ , where  $m$   
920 is the slope of the linear fit of the photoluminescence background and  $I(G)$  is the intensity of the Raman  
921 G band [53,54]. In this work, for the data collected on the impactation ROIs (the data of the halo ROIs  
922 cannot be used due to the absence of the G band),  $\log m/I(G)$  shows a linear dependence ( $R = 0.8706$ ) on  
923 [H] up to 70 mm HAB:

$$\log \frac{m}{I(G)} = -13(2) + 44(6) \times [H]$$

Equation 8.3.

924 At higher HAB, the linearity is lost. In Figure SI 4, the fitting function is compared to empirical  
925 equations obtained from the analysis of hydrogenated carbon films prepared by chemical vapor deposition  
926 [53,54]. The three empirical equations differ significantly in their slope and intercept. A likely  
927 explanation is in the different depth sensibility at the sample surface of the used diagnostic: ToF-SIMS in  
928 static mode (<1-2 nm, this work), nuclear reaction analysis (<2-5 nm, [53]) and elastic recoil detection  
929 analysis (<2-5 nm, [54]). On the other hand, even the shortest penetration depth of a Vis laser beam  
930 typically used for Raman spectroscopy on highly absorbing carbonaceous materials can be estimated in  
931 the range of a few  $\mu\text{m}$  [98]. Therefore, caution should be paid when using these equations since they  
932 compare desorption-related phenomena inherently linked to the material surface to interactions occurring  
933 nearly in the bulk.

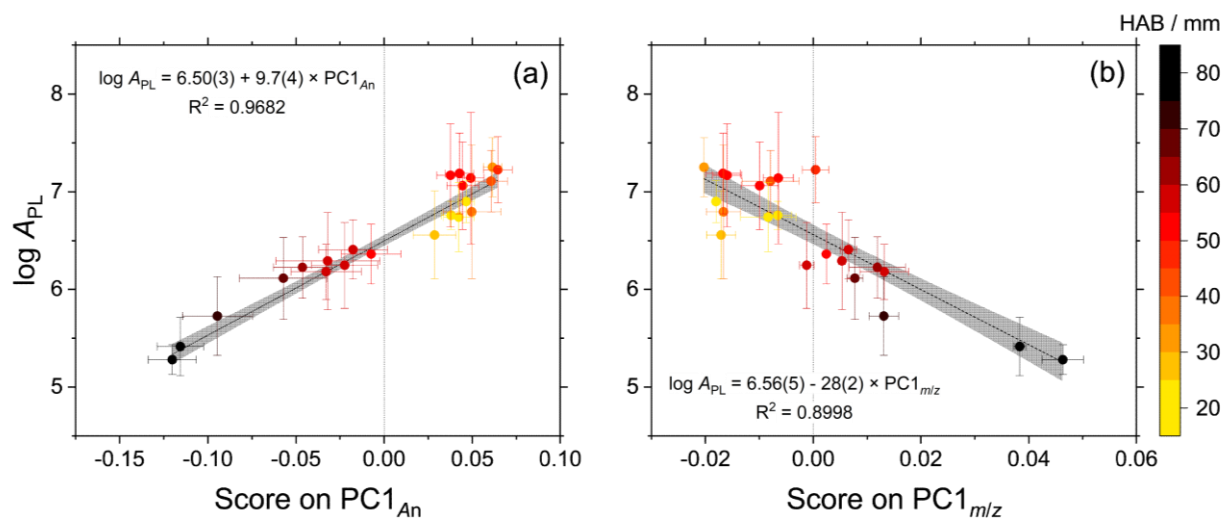


934  
 935 **Figure SI 4.  $\log m/I(G)$  against  $[H]$ .** The linear fitting does not include 80-100 mm HAB datapoints, for which the linear  
 936 correlation is lost. The 95% confidence band is shown (gray area). Two equations obtained from the analysis of  
 937 amorphous hydrogenated carbon films prepared by chemical vapor deposition [53,54] are shown by comparison.  
 938

## 939 8.6 The Raman photoluminescence background

940 In the Raman spectra, the integrated photoluminescence area  $A_{PL}$  is considered to be proportional to the  
 941 local concentration of condensable species deposited on the substrate and fluorescing when excited at  
 942 514.5 nm. As shown in Figure SI 5,  $\log A_{PL}$  is linearly correlated to both  $PC1_{An}$  and  $PC1_{m/z}$ .  $A_{PL}$  decreases  
 943 by one order of magnitude at 53-54 mm HAB, which corresponds to the transition to the second cluster of  
 944  $PC1_{An}$  in Figure 4.  $A_{PL}$  remains constant up to 60 mm HAB then decreases by another order of magnitude  
 945 in 65-80 mm HAB samples, in accordance with the transition to the third cluster of  $PC1_{An}$ . Therefore,  
 946 peaks D5, D3 and G and  $A_{PL}$  are linked to the presence of high  $m/z$  hydrocarbons. In particular, high  $m/z$   
 947 hydrocarbons in the mass spectra correspond to weak peak D3, intense peaks G and D5 and high  $A_{PL}$ .  
 948 Conversely, the absence of high  $m/z$  hydrocarbons from the mass spectra corresponds to intense peak D3,  
 949 weak peaks G and D5 and low  $A_{PL}$ . The  $A_{PL}$  spanning two orders of magnitude can be a consequence of

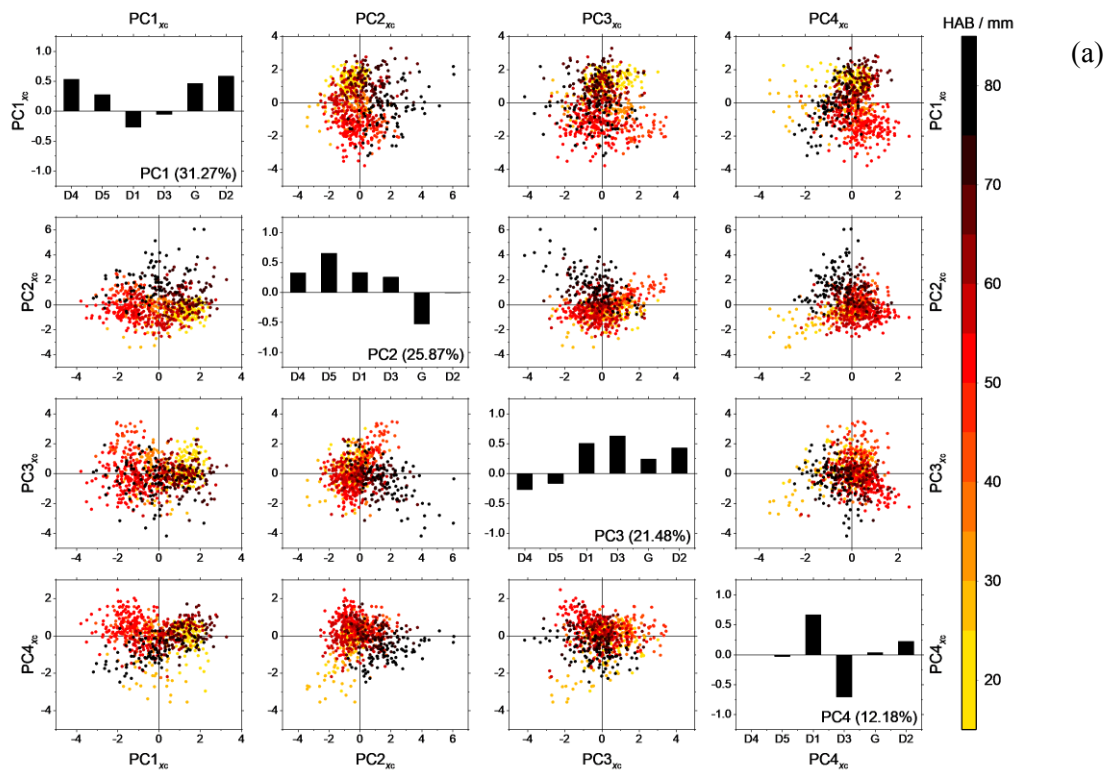
950 changes in the concentration in the gas phase or the deposition efficiency of the condensable  
951 hydrocarbons.



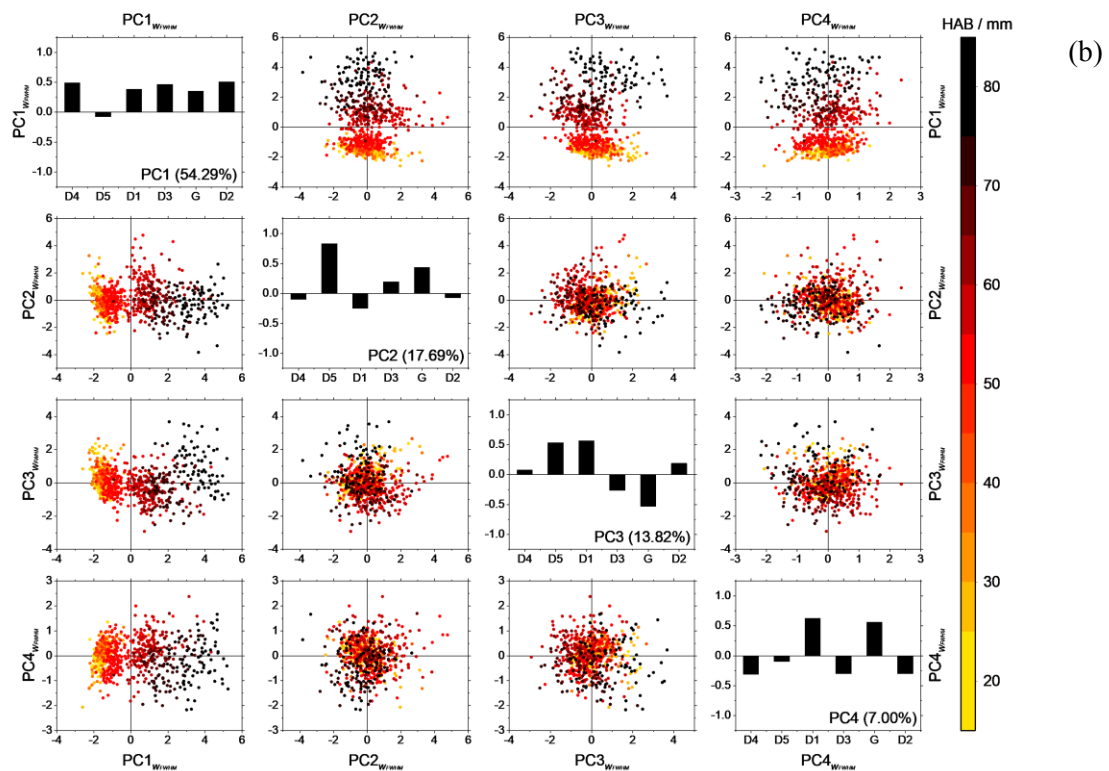
952

953 **Figure SI 5. Dependences of the integrated photoluminescence area.**  $A_{PL}$  against (a) scores on  $PC1_{An}$ , and (b) scores  
954 on  $PC1_{m/z}$ . The linear fittings (black dashed lines) and the 95% confidence interval (gray areas) are shown.

955

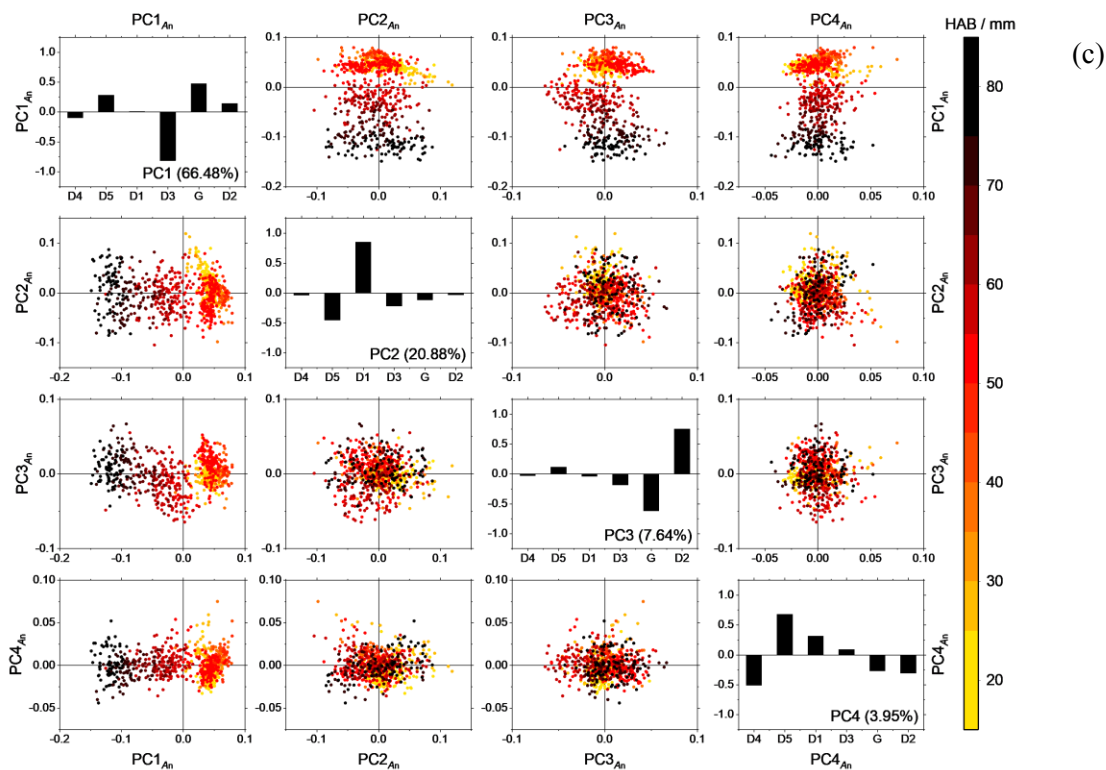


957



958





959

960 **Figure SI 6. Results of the PCA performed on the Raman spectral parameters on the impaction ROIs.** (a) peak  
 961 positions  $x_c$  and (b) peak widths  $w_{FWHM}$  (different scales, correlation matrix is used). (c) normalized areas  $A_n$  (similar  
 962 scale, covariance matrix is used). The figures show the score plots of the first four principal components and the  
 963 corresponding loading plots in the main diagonal. The scores are color-mapped on the sampling HAB (the colormap scale  
 964 is on the side).

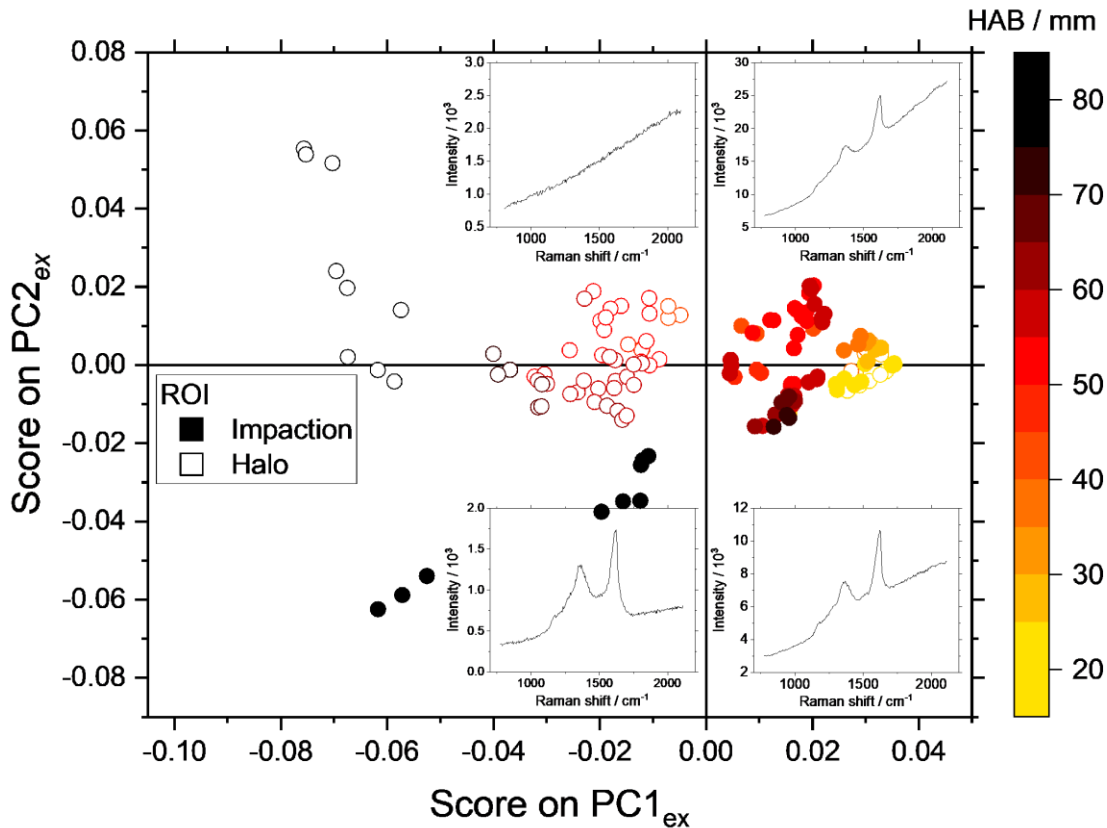
965

## 966 8.8 Exploratory data analysis

967 Exploratory PCA is performed on the totality of the mass spectra after removing the background and  
 968 fragment ions (covariance matrix, 520  $m/z$  values as variables, 150 mass spectra as observations). As a  
 969 rule of thumb, adding information to the score plots helps the principal components related to physical  
 970 phenomena, while the loading plots pinpoint the variables affecting the respective principal components.  
 971 Figure SI 7 shows the  $PC2_{ex}$  against  $PC1_{ex}$  score plot of the exploratory analysis including all available

972 information on the sampling HAB and analysis ROI. The corresponding Raman spectra are shown in the  
973 insets.

974 At 13-35 mm HAB (yellow datapoints), no statistically significant differences are found between the  
975 mass spectra of the impaction and halo ROIs that appear closely clustered together with high positive  
976 scores in  $PC1_{ex}$ . At 40-70 mm HAB, the mass spectra of the impaction and halo ROIs are split into  
977 different data clusters in  $PC1_{ex}$ : the impaction ROIs have positive scores on  $PC1_{ex}$  (red-brown solid  
978 datapoints) while the halo ROIs have negative scores on  $PC1_{ex}$  (red-brown hollow datapoints). In this  
979 HAB range, Raman spectra are detected only in the impaction ROIs but not in the halo ROIs. At  
980 80-100 mm HAB, the mass spectra of the impaction and halo ROIs are found scattered with negative  
981 scores in  $PC1_{ex}$ . The impaction ROIs have high negative scores on  $PC2_{ex}$  (black solid datapoints) while  
982 the halo ROIs have low negative or positive scores on  $PC2_{ex}$  (black hollow datapoints). Again, Raman  
983 spectra are detected only in the impaction ROIs but not in the halo ROIs.



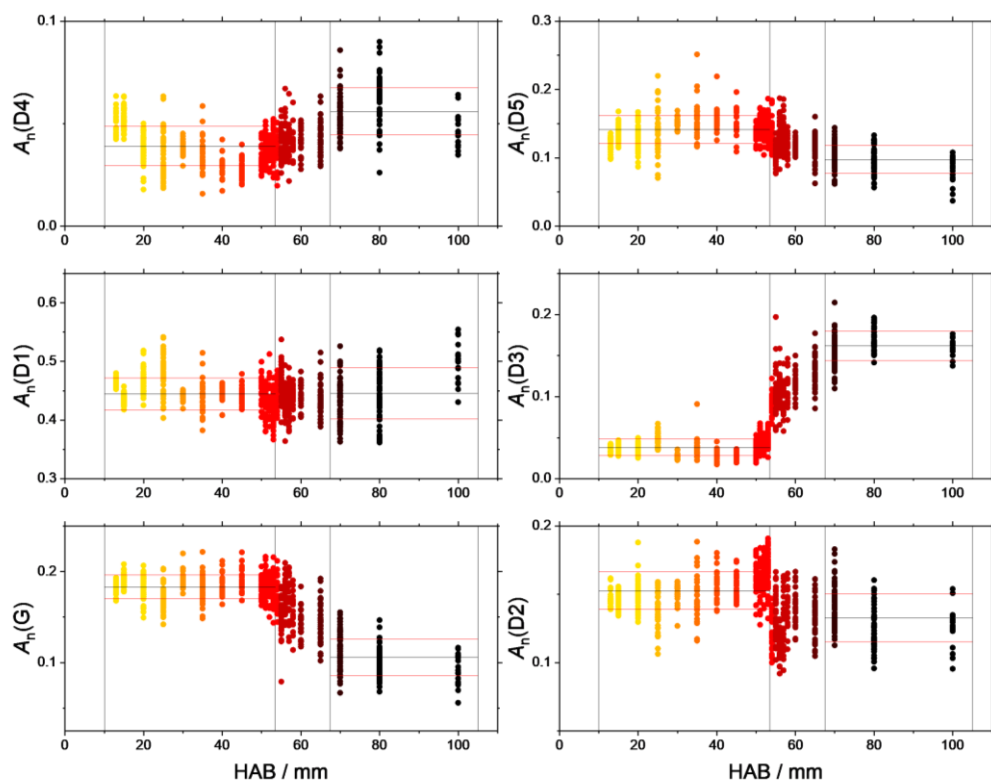
984

985 **Figure SI 7. Exploratory data analysis.** PC2<sub>ex</sub> against PC1<sub>ex</sub> score plot, all mass spectra in the database included. The  
986 datapoints color and interior represent the sampling HAB and the analysis location on the substrate (solid, impaction  
987 ROIs and hollow, halo ROIs), respectively. (b) The corresponding Raman spectra are shown in the insets.

988  
989 From the analysis of the score plot in Figure SI 7, decreasing scores in PC1<sub>ex</sub> correspond to the  
990 progressively increasing sampling HAB, but also to a rather net data clustering of the impaction and halo  
991 ROIs. The phenomena responsible for this data clustering are associated with the HAB and ROI change,  
992 with the former likely related to the flame chemistry and the latter possibly related to a phase repartition  
993 during the sampling [35,49]. To focus on the flame chemistry only, the PCA is performed again on the  
994 impaction ROIs only (*Results 3.1*). However, the halo ROIs also contain information useful for  
995 understanding the formation of incipient soot particles.

996

## 997 8.9 Dependences of the Raman spectral parameters

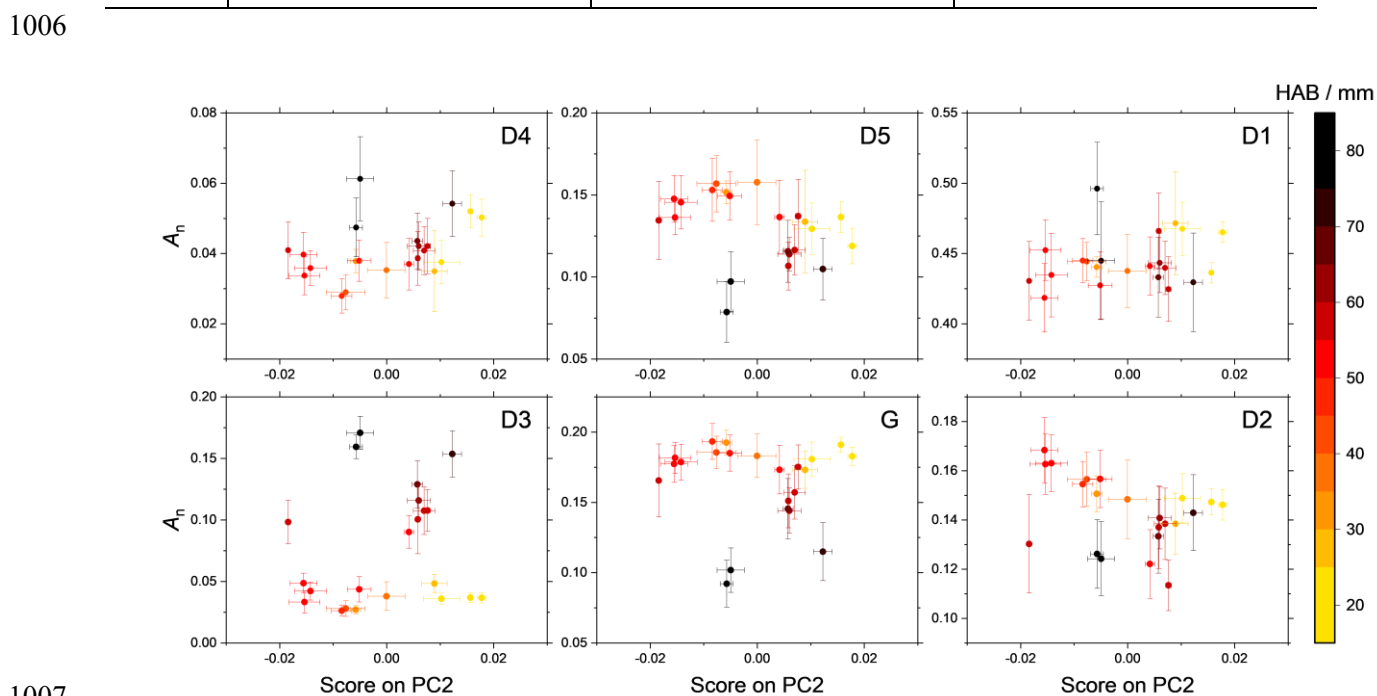


998

999 **Figure SI 8.** Dependence of the peak normalized areas  $A_n(X)$  on the HAB. The horizontal black and red lines represent the  
1000 average and  $\pm 1$  standard deviation, respectively, calculated upstream (15-53 mm HAB) and downstream (70-100 mm  
1001 HAB) the flame transition region (54-60 mm HAB), and given in Table SI 2. The data are color-mapped on the sampling  
1002 HAB.  
1003

1004 **Table SI 2.** Average values of the fitted spectral parameters calculated upstream (15-53 mm HAB) and downstream  
 1005 (70-100 mm HAB) the flame transition region (54-60 mm HAB). The uncertainty represents one standard deviation.

	$x_c / \text{cm}^{-1}$			$w_{\text{FWHM}} / \text{cm}^{-1}$			$A_n$		
	15-53 mm	70-100 mm	Difference	15-53 mm	70-100 mm	Difference	15-53 mm	70-100 mm	Difference
D4	1170±3	1172±5	2±6	51±6	98±20	47±21	0.04±0.01	0.06±0.01	0.02±0.02
D5	1255±4	1265±7	10±8	118±10	113±12	5±16	0.14±0.02	0.10±0.02	0.04±0.03
D1	1363±5	1361±2	2±5	112±7	129±12	17±14	0.45±0.03	0.45±0.04	0.00±0.05
D3	1517±14	1522±13	5±19	99±14	162±12	63±18	0.04±0.01	0.16±0.02	0.12±0.02
G	1594±2	1590±3	4±4	50±2	55±4	5±4	0.18±0.01	0.10±0.02	0.08±0.02
D2	1618±1	1618±2	0±1	29±2	41±4	12±4	0.15±0.01	0.13±0.02	0.02±0.02



1008 **Figure SI 9.**  $A_n$  against scores on  $\text{PC2}_{m/z}$ . Notice that, since it was not possible to perform the two analyses on the same  
 1009 locations on the sample surface, the average and standard deviation calculated on all available data are used instead.

1010